Atmospheric
Measurement
Techniques
Open Access

Discussions

Satellite retrieval of aerosol microphysical and optical parameters using neural networks: a new methodology applied to the Sahara desert dust peak

M. Taylor[1], S. Kazadzis[1], A. Tsekeri[2], A. Gkikas[3], and V. Amiridis[2]

[1]Institute for Environmental Research and Sustainable Development (IERSD), National Observatory of Athens (NOA), Metaxa & Vas. Pavlou, Penteli, 15236, Athens, Greece
[2]Institute for Astronomy, Astrophysics, Space Applications and Remote Sensing (IAASARS), National Observatory of Athens (NOA), Metaxa & Vas. Pavlou, Penteli, 15236, Athens, Greece
[3]Laboratory of Meteorology, Physics Department, University of Ioannina, Greece

Correspondence to: M. Taylor (patternizer@gmail.com)

Discussion Paper | Discussion Paper | Discussion Paper | Discussion Paper

Title Page

Abstract | Introduction

Conclusions | References

Tables | Figures

◄◄ | ►►

◄ | ►

Back | Close

Full Screen / Esc

Printer-friendly Version

Interactive Discussion

Abstract

In order to exploit the full-Earth viewing potential of satellite instruments to globally characterise aerosols, new algorithms are required to deduce key microphysical parameters like the particle size distribution and optical parameters associated with scattering and absorption from space remote sensing data. Here, a methodology based on neural networks is developed to retrieve such parameters from satellite inputs and to validate them with ground-based remote sensing data. For key combinations of input variables available from MODIS and OMI Level 3 datasets, a grid of 100 feed-forward neural network architectures is produced, each having a different number of neurons and training proportion. The networks are trained with principal components accounting for 98 % of the variance of the inputs together with principal components formed from 38 AERONET Level 2.0 (Version 2) retrieved parameters as outputs. Daily-averaged, co-located and synchronous data drawn from a cluster of AERONET sites centred on the peak of dust extinction in Northern Africa is used for network training and validation, and the optimal network architecture for each input parameter combination is identified with reference to the lowest mean squared error. The trained networks are then fed with unseen data at the coastal dust site Dakar to test their simulation performance. A NN, trained with co-located and synchronous satellite inputs comprising three aerosol optical depth measurements at 470, 500 and 660 nm, plus the columnar water vapour (from MODIS) and the modelled absorption aerosol optical depth at 500 nm (from OMI), was able to simultaneously retrieve the daily-averaged size distribution, the coarse mode volume, the imaginary part of the complex refractive index, and the spectral single scattering albedo – with moderate precision: correlation coefficients in the range $0.368 \leq R \leq 0.514$. The network failed to recover the spectral behaviour of the real part of the complex refractive index with only 39–45 % of the data falling within the acceptable level of uncertainty relative to ground-truth data at the daily timescale. In the context of Saharan desert dust, this new methodological approach appears to

offer some potential for moderately accurate daily retrieval of previously inaccessible aerosol parameters from space.

1 Introduction

Aerosol particles reflect and absorb solar radiation in the atmosphere shading the Earth's surface. They also reduce visibility and can have a direct effect on human health (Samet et al., 2000). Moreover, they are used to determine the Earth's hydrological cycle (Remer et al., 2005). However, because of inadequate quantitative knowledge of the global spatial and temporal variation of aerosol optical properties (Hansen et al., 2005), there is uncertainty in the magnitude of their contribution to the Earth's climate and planetary radiative-forcing (IPCC, 2007). With the expansion of the global AEosol RObotic NETwork (AERONET) of high quality remote sensing measurement instruments (Holben et al., 1998) and the development of advanced and robust inversion algorithms (Dubovik and King, 2000) for the retrieval of aerosol parameters, our understanding of aerosol microphysics and optical properties has improved greatly. However, the size of the uncertainty associated with the aerosol contribution is known to be unacceptably large and must be reduced by at least a factor of 3 (Schwartz, 2004). An attempt to address this uncertainty has been outlined in a recent report (Mishchenko et al., 2007). In particular, the report presents aerosol retrieval accuracy requirements for remote-sensing instruments in space to be able to detect changes in planetary aerosol radiative-forcing over the next two decades:

– radius of the fine and coarse particle modes (±10 %)

– variance of the fine and coarse particle modes (±40 %)

– spectral behaviour of the real part of the complex refractive index, CRI-R (±0.02)

– spectral behaviour of the single-scattering albedo, SSA (±0.03).

The last parameter is a key aerosol optical property and proxy for radiative-absorption (Hansen and Travis, 1974). Retrieval of all of these parameters from inversion of direct sun and sky radiance measurements is provided by AERONET (Dubovik and King, 2000; Dubovik et al., 2002). Unfortunately, these retrievals have low and inhomoge-
5 neous spatial resolution (AERONET's ground-based remote sensing instruments are densely situated in and around cities and sparsely-located elsewhere). Furthermore, AERONET stations are largely absent from vast uninhabited areas like deserts, oceans and the ice-caps which are the largest sources of planetary aerosol. Marine aerosol retrievals, in particular, are only available at island sites or in coastal regions. In con-
10 trast, space-bound satellite instruments like the MODerate resolution Imaging Spectro-radiometer (MODIS) instrument on board the satellites Terra and Aqua, sample the vertical atmospheric column of the whole Earth, but their retrieval algorithms are not currently able to provide reliable proxies containing information on the mean particle size of fine and coarse aerosol, the complex refractive index and particle shape – all
15 necessary for a full understanding of aerosol microphysics (Remer et al., 2005) and for globally-characterizing different types of aerosols and sources (Tanré et al., 1996). Therefore, in order to exploit the full-Earth viewing potential of space-bound measurements, new algorithms are required to deduce these key parameters.

1.1 Motivation

20 With the measurement accuracy requirements of Mishchenko et al. (2007) above providing the context, this paper focuses on the question of how to retrieve daily estimates of all of these parameters from satellite measurements. In this paper, we assess the potential for achieving this by constructing neural network (NN) models and applying them to data from an extensive region (Northern Africa) – where the dust global aerosol
25 optical depth (AOD) has its peak (Chin et al., 2002).

This work is motivated then by the potential offered by capitalizing on the full-Earth coverage of AOD, H_2O and AAOD provided by satellite remote sensing instruments together with AERONET-quality retrievals of the aerosol volume size distribution (AVSD),

CRI, SSA, and the particle asymmetry factor (ASYM). The key to building the required bridge between ground and satellite retrievals is to train NNs on AERONET "ground-truth" data so as to learn the relationship between combinations of satellite AOD, H_2O and AAOD inputs and AERONET microphysical and optical parameters as outputs. The potential of the NNs to extrapolate is then tested by feeding them with unseen satellite inputs and comparing the outputs against co-located and synchronous ground-based AERONET data. In our study, we use the latest AERONET Level 2.0 Version 2 Inversion Products that are cloud-screened and quality assured (AERONET, 2012).

1.2 Contemporary studies

In the last 5 yr or so, multivariate fitting techniques including function-approximating NNs have been brought to bear on problems in the field of aerosol science. Of paramount importance is the finding that a characteristic aerosol fine mode volume and effective radius can be derived from measurements of the AOD, the Ångström Exponent (å) and its curvature using a multi-functional approach (Gobbi et al., 2007). A further study constructed a multiple-input single output NN that took radiances, solar viewing angles, and terrain elevation from MODIS as input, and predicted the values of co-located AERONET AOD values as output (Radosavljevic et al., 2010). The study used data from 221 AERONET sites and demonstrated that AERONET AOD could be successfully estimated from satellite inputs. NN models were also applied in a very recent study designed to detect and retrieve volcanic ash cloud properties from multi-spectral infrared MODIS measurements over Mount Etna during recent volcanic eruptions (Picchiani et al., 2011). These studies are a sign that the aerosol community is starting to embrace such methods.

AERONET's latest Level 2.0 Version 2 inversion algorithm retrieves all of the afore-mentioned aerosol microphysical and optical parameters from ground-based sensors by performing multivariate regression – which must be performed for each measurement. On the contrary, the NNs are potentially able to simultaneously retrieve the AVSD, CRI, SSA, and ASYM for the entire data sample in a single step – without having to

recalculate each day. NN retrieval schemes therefore (potentially) have the capacity to produce real-time retrievals for large datasets. To be more specific, the NN calculates the inverse function (applying to all cases covered by the training space), whereas other methods like look-up table and optimal estimator methods match aerosol properties to corresponding light measurements for every case separately. The calculation of the inverse function may require considerable time in the case of a NN due to the need for running a grid of training NNs, but, once complete, the retrieval using the trained optimal NN is instantaneous. The theoretical basis underpinning the NN function approximation scheme is presented in Sect. 3.1.

1.3 Objectives

Motivated by the need to develop a methodology to produce global satellite retrievals of aerosol microphysical and optical parameters, and inspired by the success of recent NN models, this paper reports on the initial phase of AEROMAP, a two-year EU-funded project that began in March 2012. This, our first major study, has the following main objectives:

1. to assess the potential of performing aerosol typing a priori by using GOCART model outputs to select suitable desert dust sites at the peak of dust extinction in Northern Africa,

2. to see if it is possible to standardize and optimize NN architectures capable of learning the relationship between the inputs and outputs for this region (i.e. for this aerosol type) and,

3. to validate the trained NNs with unseen data at a distant geo-location in the same region (i.e. aerosol type), and to assess their performance using statistical regression and timescale analysis.

1.4 Structure of the paper

The data used and an outline of the NN model are presented in Sect. 2. Section 3 then presents the theory involved in training and validating such NNs. In Sect. 4, the results of NN training and testing for different input configurations are presented and key find-
ings, major impacts, as well as pros and cons of the method are noted and analyzed in Sect. 5. Finally, we conclude in Sect. 6 by assessing the overall potential offered by the NN methodology for retrieving aerosol microphysical and optical parameters from space.

2 Methodology

Aerosol particles from different sources have different sizes, absorption properties, and shape. They are typically classified into a small number of types ($\approx$ 5–10) including for example: desert or soil dust, smoke or organic and black carbon from biomass burning, urban sulphates, marine sea salt, volcanic ash as well as their mixtures. Researchers in the field have found that different aerosol types correlate strongly with pairs of different aerosol parameters, but no consensus has yet been reached on a single method to disambiguate and universally-distinguish them. Therefore, in this work, in order to avoid as much as possible such potential sources of data inhomogeneity or inconsistency, we adopted an independent qualitative approach to aerosol typing which is described in Sect. 2.1.3.

2.1 Data selection

This work draws on 4 different data sources: "satellite inputs" from MODIS and the Ozone Measuring Instrument (OMI), ground-based remote sensing data from AERONET, and global chemical model output data from the Georgia Institute of Technology–Goddard Global Ozone Chemistry Aerosol Radiation and Transport (GO-CART) model (Chin et al., 2000, 2002, and Ginoux et al., 2001). MODIS and OMI

provide satellite inputs and co-located and synchronous values of these inputs as well as output parameters at the ground are provided by AERONET. GOCART data is used for aerosol typing.

2.1.1 Satellite inputs

MODIS on board the Terra (EOS-AM) and Aqua (EOS-PM) satellites has been capturing data in 36 spectral bands from 400 nm to 1440 nm since 1999 with a spatial resolution ranging from 250 m–1 km. Collectively, the instruments image the entire Earth surface every 1–2 days. Daily-averaged data was downloaded in hierarchical data format from the MODIS Level 3 Collection 5.1 Product (MODIS, 2012). From these files, AOD(470), AOD(550), AOD(660) time series provided at 1° × 1° spatial resolution were extracted. In addition, co-located and synchronous, Level 2, near-infrared, mean total columnar water vapour (H_2O) from the Aqua satellite (dataset MYD05_L2) was also downloaded. Finally, the daily estimate of near-ultraviolet (UV) AAOD(500) was downloaded from the OMI Level 3 OMAERUV Product (OMI, 2012) for co-located and synchronous data (with MODIS) to test the impact of absorption on NN retrieval quality. As a result, daily-averages of these parameters were obtained for the entire global domain, spanning the full temporal record of available data: 4 July 2002 to 4 July 2012.

2.1.2 AERONET retrievals

The AERONET Level 2.0 Version 2 Inversion Products contain retrievals for 116 different aerosol parameters including the AVSD: $dV(r)/d\ln r$ (in $\mu m^3 \mu m^{-2}$) retrieved in 22 logarithmically-equidistant radial bins spanning the range of particle radii: $0.05 \mu m \leq r \leq 15 \mu m$, the real and imaginary parts of the refractive index: CRI-R(λ), CRI-I(λ), and the optical parameters: AOD(λ), SSA(λ), and ASYM(λ) centered at 4 wavelengths: $\lambda = 440$, 675, 870 and 1020 nm. Daily-averaged retrievals were downloaded for the entire global AERONET record (comprising 809 sites) and spanning the period: 1 March 1996 to 7 April 2012. For each site, its elevation (height above sea level in meters), its Eastern

Full Screen / Esc

Printer-friendly Version

Interactive Discussion

longitude and Northern latitude were extracted. In addition, although AERONET's Level 2.0 Version 2 Inversion Products also provides the mean geometric radii of the fine and coarse modes: $r(f)$ and $r(c)$, their standard deviations: $\sigma(f)$ and $\sigma(c)$, and their volume concentrations: $V(f)$ and $V(c)$, the fine fraction η which is not provided – was also calculated and appended to the AERONET data record. All of these parameters are calculated from the AVSD by specifying a mode separation point r_s and, in what follows, we will refer to them collectively as secondary microphysical parameters. Their calculation (required for comparing satellite-driven NN simulated outputs with AERONET) is described briefly in Appendix A. Furthermore, while the vast majority of AERONET stations provide AOD data at the central wavelengths: 440, 675, 870 and 1020 nm, it has been found that there is a (small) difference between AODs obtained by MODIS and AERONET which is important and non-negligible (Remer et al., 2005). Hence, the Ångström Exponent å(675 nm/440 nm) was calculated and used to extrapolate AERONET AODs to match those available from space at MODIS wavelengths with the rearrangement:

$$AOD\,(\lambda_2) = AOD\,(\lambda_1) \left(\frac{\lambda_2}{\lambda_1}\right)^{-\text{å}(\lambda_2, \lambda_1)} \qquad (1)$$

These interpolated-AERONET AOD(470), AOD(550), AOD(660) values were also appended to the AERONET dataset. This dataset therefore contains both ground retrievals of the satellite inputs (aligned to the central wavelengths provided by MODIS) plus the output parameters which the NN model is built to retrieve.

2.1.3 Aerosol typing

In order to isolate suitable desert dust data for this study, we developed a qualitative 2-step approach. In the first step, the AERONET dataset was ranked by the number of complete records available at each site (without data gaps in the input parameters: AODs, H_2O, AAOD, and the output parameters: AVSD, CRI-R, CRI-I, SSA and ASYM).

The requirement for records to be complete caused the number of sites to drop from 807 to 623 sites. It was found, for example, that the top-ranked site in the study region (Northern Africa) is Banizoumbou (Niger) which contains 2283 complete data records. The second step of our approach aims to answer the question: how many of these daily-averaged records are dust dominated? For this, the GOCART model AOD extinction per aerosol type was used. GOCART provides 3 hourly measurements of the total extinction AOD as well as the contribution to total extinction AOD of sulphate (SO_2), organic carbon (OC), black carbon (BC), desert (mineral) dust and sea salt. GOCART data was downloaded for the first 155 AERONET sites ranked in step 1 by the number of complete records. This list accounts for 75 % of all available Level 2.0 Version 2 inversions. Since GOCART provides eight 3 hourly measurements per day, these were averaged to produce daily-averages and expressed as a percentage of the total extinction AOD for each aerosol type. The percentage of dust was then used as a basis for re-ranking the list of high data volume sites. Table 1 below shows the AERONET "complete record", "ranked-sites", ranked by dust contribution (according to GOCART data) for the study region (Northern Africa).

In Table 1, "Dataset A" comprises AERONET sites that operate the older CIMEL model I sun photometers which lie on the peak of dust AOD extinction as extracted from the mean global GOCART model output, and which are verified via cross-reference with the strongest TOMS dust sources (shown in Fig. 1 below). "Dataset B" comprises those sites that operate the newer CIMEL model II sun photometers which, in addition, also contribute measurements of near-UV AOD at 380 nm and 500 nm. This separation of the Northern Africa data was made so as to investigate the possible effect of UV AOD inputs on NN model performance. Dakar was selected as the testing site since: (i) it has the largest number of days of co-located synchronous satellite measurements, (ii) it is also located on the peak of dust AOD extinction, and (iii) it operates the newer model II CIMEL sun photometer.

2.1.4 Handling of outliers

While it is generally not good practice to remove outliers since they often correspond to interesting phenomena, in relation to NNs, it is important that infrequently-occurring, extreme data that can significantly bias the data-fitting procedure is removed. This led us to investigate various methods of outlier detection and to study the distribution of the data for each of the input and output parameters. Histograms were produced that partitioned the data into 20 bins and it was found that all many of the parameters presented near-normal distributions in quantile-quantile plots (the H_2O, the volume concentration in each radial bin, the CRI-R and the ASYM), but that AODs and the CRI-I presented positive skew-normal distributions, and the SSA presented negative skew-normal distributions. We elected to apply the Grubb's Test (Grubbs, 1969) to remove outliers. Grubb's Test consists of testing one data point at a time and finding and removing the value furthest from the sample mean (usually applied to normally-distributed data). Since the median is more statistically-robust when analyzing data that is skew-normal, Grubb's Test was applied with reference to the sample median rather than the sample mean. This procedure was applied iteratively to Datasets A and B (used to train the NNs) until outliers were removed at the 68 % confidence level of the entire 2-tailed data distribution. Outliers were deliberately not removed from the inputs used in testing the NN so that the ability of the NNs to extrapolate on raw, unseen data could be properly tested. The data selection scheme produced dust-typed input-output data that: (a) is homogeneous (does not contain parameter data gaps), (b) is wavelength-matched and (c) is free of biasing values (at the 68 % level of confidence).

2.2 The NN model

Feed-forward NNs having at least one layer of "hidden" neurons whose activation functions, are nonlinear hyperbolic tangent (Tanh) functions (or other general nonlinear sigmoidal functions), are able to operate as universal function approximators (Cybenko, 1989; Hornik, Stinchombe and White, 1989). This means that, given enough hidden

neurons and training data, such networks are capable, in principle, of learning the mathematical relation between inputs and outputs. The input and output parameters used in this work were connected via 2 network layers – the first layer containing hidden neurons with Tanh activation functions and the second layer containing output neurons having linear activation functions. We also tested 3-layer models that used 2 layers of hidden neurons but the results were worse than those obtained here. The relation between input and output parameters for the type of NN used in this study is presented in Sect. 3.1, together with details of the methodology adopted for evaluating network training (Sect. 3.2) and network validation (Sect. 3.3). Here, we describe the operation of the NN model which was coded using MATLAB's object-oriented scripting language in conjunction with its neural network toolbox (Demuth and Beale, 2004).

NN models require specification of: (1) how the performance error associated with the network model is to be measured, and (2) the architecture used. We measure the performance error of the network using the mean squared error (MSE) calculated from the difference between its outputs and target output data. The details of the macro-statistical approach we adopt are presented in Sect. 3.2 in the context of NN training. The NN architecture is a more complex entity. It involves not only the number of hidden neurons and their activation functions, but also the proportion of data used to train and validate the NN as well as the learning algorithm used. The perception that NN models are somewhat subjective is due to what is often seen as an arbitrary choice of some or all of these elements. In order to try to make the choice of architecture more objective, we developed a new procedure to detect optimal NN architectures. We began by creating a list of candidate input-output combinations (see below). Then, we trained the corresponding NNs by following four steps:

1. normalize all input and output variables,

2. apply principal components analysis (PCA) to inputs and outputs separately so as to exclude redundant variability (it is required that the PCs account for 98 % of the total variance),

3. loop through a grid of 100 NNs of varying numbers of hidden neurons (4–24 in steps of 2) and proportions of training data (40–90 % in steps of 5 %), and

4. select the NN that has the minimum total training and validation MSE.

This procedure can be automated and was found to avoid the bias and under-fitting that can result from having too few neurons on the one hand, and the high variance and over-fitting that can result from having too many on the other (see Sect. 3.2). It also avoids arbitrary partitioning of the data into training and validation proportions, and the use of PCA helps exclude redundant variability which can adversely affect training efficiency (Jolliffe, 2002). While we are conscious that the components calculated from PCA are a mixture of the original variables and should not be applied indiscriminately (potentially producing non-physical combinations), we also did some trials applying PCA on groups of variables of the same type (e.g. AVSD bins and spectral parameters separately) so as to retain physical characteristics within variable clusters – but the results were worse than those presented here.

Regarding candidate input combinations, we drew up a list of aerosol parameters which are provided by satellites globally at $1° \times 1°$ spatial resolution, leading to the following set: AOD(470), AOD(550), AOD(660) and H_2O from MODIS, and AOD(380), AOD(500) and AAOD (500) from OMI. Since it has been suggested that there is high sensitivity to particle absorption in the near-UV (Torres et al., 2002), it was decided that this effect would be studied separately by constructing an input combination that depended on the near-UV AOD at 380 nm and 500 nm – which are provided by the new CIMEL (model II) AERONET sun photometers comprising Dataset B. Note that the AAOD(500) provided by OMI is a modelled parameter obtained by using a look-up table of expected SSA values that depend on the aerosol type and the geographical location (Torres et al., 2007). Conversely, in the case of AERONET, the value of AAOD (at the central wavelengths: 440, 675, 870 and 1020 nm) is calculated from retrieved aerosol microphysical properties (Dubovik et al., 2000). In all, the following 4 distinct scenarios were identified and used in this study:

- CASE 1 inputs = AERONET: AOD(470), AOD(550), AOD(660)

- CASE 2 inputs = AERONET: AOD(470), AOD(550), AOD(660) + H_2O

- CASE 3 inputs = AERONET: AOD(470), AOD(550), AOD(660) + H_2O + AOD(380), AOD(500)

- CASE 4 inputs = MODIS: AOD(470), AOD(550), AOD(660) + H_2O and OMI: AAOD (500)

In each case, the set of output variables comprises: the AERONET microphysical AVSD (calculated at 22 equidistant logarithmic radial bins spanning the range 0.05 µm to 15 µm), the spectral refractive index and the optical parameters SSA and ASYM centred at 440, 675, 870 and 1020 nm. CASES 1 and 2 use daily-averaged records drawn from Dataset A, CASE 3 uses daily-averaged records drawn from Dataset B and CASE 4 uses co-located satellite data synchronous with Dataset A (see Table 1). The NN model then proceeds as follows. PCA is applied to the input and output data separately for each of the CASES 1–4 and a grid of 100 NNs of differing (hidden neuron, training%) architecture is produced, trained and validated. The optimal NN is then identified using the minimum total training and validation MSE between the NN outputs and target AERONET data. The PCA is inverted back to parameter space and comparative (linear regression) statistics are calculated for the outputs of the optimal trained NN in relation to the AERONET training output data. In order to test each optimally-trained NN, new and unseen CASE 1–4 data at the coastal dust site Dakar is transformed into PCA space and fed to the corresponding NNs. In each case, the network's output is transformed back from PCA space to parameter space where comparative statistics are again applied to the NN outputs in relation to AERONET "ground-truth" data. A schematic of the overall NN model is shown in Fig. 2.

In Sect. 3, the functional relation between network outputs and inputs is presented together with details of the methods used to train and validate the performance of the NNs.

3 Theory

3.1 The NN input-output function approximation

As we discussed in Sect. 2.2, the motor behind the NN model is the multiple input, multiple output 2-layer feed-forward NN at the centre of Fig. 2. The NN has the following
5 input–hidden layer–output layer connectivity shown in detail in Fig. 3.

The NN has a vector X of R-input PCs and a vector Y of s^2-output PCs (grey circles). For CASE 4 for example, PCA applied to the inputs generated $R = 3$ PCs, and PCA applied to the outputs produced $s^2 = 7$ PCs (see Sect. 2.2 for details). The NN has 2 layers of neurons connecting the inputs to the outputs. The first layer (the "hidden"
10 layer) has s^1 neurons with nonlinear activation functions $f^1 = $ Tanh and the output layer has s^2 neurons with linear activation functions f^2. Each neuron has a single bias [0,1] and so the hidden layer has a vector b^1 of s^1 biases while the output layer has a vector b^2 of s^2 biases. The vector of R-inputs X is connected to the s^1-neurons of the hidden layer via a matrix of $[s^1 \times R]$ input weights $\mathbf{IW}^{1,1}$ while the vector a^1 of s^1-outputs is
15 connected to the s^2-output neurons via a matrix of $[s^2 \times s^1]$ layer weights $\mathbf{LW}^{2,1}$. Finally, the vector a^2 of s^2-outputs is the vector Y of NN outputs. The *exact* mathematical equation relating the NN outputs to the NN inputs is then the matrix equation:

$$Y = f^2 \left(\mathbf{LW}^{2,1} f^1 \left(\mathbf{IW}^{1,1} X + b^1 \right) + b^2 \right). \tag{2}$$

20 The multiplication of the matrix $\mathbf{IW}^{1,1}$ and the vector X is a dot product equivalent to the summation of all input connections to each neuron in the hidden layer. Equation (2) above is the nonlinear functional approximation N that relates the output parameters to the input parameters:

$$Y = N(X). \tag{3}$$

25 As we described in Sect. 2.2, the input vector X contains a combination of the satellite input parameters while the output vector Y contains the sought-after retrievals.

Traditionally, a NN is assessed by dividing available data into 3 proportions: a training set, a validation set, and a testing set. However, since the data reduction scheme described in Sect. 2 led to a substantial loss of available data records, it was decided that all available data should be put to use in NN training and validation, with none reserved for testing. During the testing phase, the NNs therefore are presented with unseen input data at a new site (Dakar) in the same region (Northern Africa), and used to simulate the outputs – i.e. they are "blind" to the expected outputs. In this way, all available aerosol-typed data for the region of interest is used (apart from Dakar) in the training and validation process and testing is able to shine light on the potential of the trained and validated NNs to work properly with unseen data. The results of the (supervised) NN training and validation phase are presented below. In Sect. 4 the results of the (unsupervised) NN testing (simulation) phase are presented.

3.2 NN training

In "supervised mode" (the training phase) batch runs are performed on a grid of 100 NNs permuting through a range of architectures such that the number of hidden neurons ranged from 4–24 (in steps of 2) and so that the training proportion ranged from 40 % to 90 % (in steps of 5 %). The NN connection weights and biases are updated (i.e. trained) using an optimization learning algorithm. Initial tests were made with both a single layer of hidden neurons and also with 2 layers of hidden neurons. For each of these tests, 4 different optimization learning algorithms were also investigated: (i) the Levenberg–Marquardt (LM) back-propagation optimisation learning algorithm (Levenberg, 1944; Marquardt, 1963) (MATLAB flag "trainlm"), (ii) Bayesian regularization (MATLAB flag "trainbr"), (iii) resilient back-propagation (MATLAB flag "trainrp"), and (iv) scaled conjugate-gradient back-propagation (MATLAB flag "trainscg"). The best results were obtained with the LM algorithm applied to a single layer of hidden Tanh neurons. During each iteration of the learning process, the weights and biases are tuned so as

to minimize the MSE cost function:

$$\text{MSE} = \frac{1}{N} \sum_{i=1}^{N} (t_i - y_i)^2. \tag{4}$$

Note that the MSE is calculated from N output vectors y_i against N AERONET target vectors t_i. Training proceeds through a number of epochs until the MSE between NN outputs and AERONET targets (expected outputs) is minimised. In particular, the MSE obtained from the training data and the MSE obtained from the validation data were summed for each NN in the grid. The optimal NN was identified as the one whose architecture had the smallest total MSE. Table 2 shows the results of applying this optimisation process to CASES 1–4.

For example, the optimal CASE 4 NN, trained with data from satellite inputs and outputs from the AERONET stations comprising Dataset A, has 22 neurons in the hidden layer, 7 neurons in the output layer, and used 90 % of Dataset A for training and 10 % for validation. This NN has 3 inputs: the 3 principal components (PCs) of AOD(470), AOD(550), AOD(660), H_2O and AAOD(500), and 7 outputs: 7 PCs of the 22 logarithmically-equidistant radial bins of the AVSD and the CRI-R, CRI-I, SSA and ASYM spectral parameters centred at 440, 675, 870 and 1020 nm. The evolution of the optimization process as well as the statistics associated with this optimal CASE 4 NN found are shown in Fig. 4.

Figure 4a shows (as expected) that the training MSE tends to decrease as the number of hidden neurons is increased, and decreases at a slower rate for larger samples of training data. Figure 4b shows that the validation MSE shows an opposite tendency – increasing slowly with the number of hidden Tanh neurons. Two sharp peaks at (*10*, 60 %) and (*20*, 45 %) are probably due to the fact that over-fitting is occurring at these points due to the small size of the dataset. The total training time is seen in Fig. 4c to increase sharply and non-linearly when the number of neurons is > 22. In relation to the evolution of NN performance with epoch in Fig. 4d, convergence has clearly been reached after 10 epochs (iterations) at the horizontal asymptote where the "Best" Validation MSE = 0.719. For all NNs, the goal for the back-propagation cost function

Title Page

Abstract | Introduction

Conclusions | References

Tables | Figures

◄ | ►

◄ | ►

Back | Close

Full Screen / Esc

Printer-friendly Version

Interactive Discussion

is set to 1/100th of the variance of the targets (for the optimal CASE 4 NN this is equal to 0.12). In this case, the goal is very stringent and is unlikely to be reached with an increase in the number of iterations – suggesting that a much larger and uniform training dataset is required to improve the training performance further. We base our interpretations in this work mostly on macro-scale statistics so as not to distract from the main goal of the study. We will consider intrinsic NN errors and uncertainty in more detail in a future paper. The Pearson product-moment correlation coefficient calculated from NN PC outputs and AERONET training PC targets for the optimal CASE 4 NN is $R = 0.992$ (see Fig. 4e) and is suggestive of an excellent NN fit. This is further backed up by histogram of the differences between NN PC outputs and AERONET training PC targets (Fig. 4e) which presents a sharply-peaked Gaussian having a near-zero mean error = 0.0006 and a standard deviation (SD)= 0.0627. These macro-statistics suggest that the optimal NN is generally well trained and performing properly the function approximation between inputs and outputs. More transparency can be gained by performing comparative macro-statistics on the output parameters separately, as described in the next section.

3.3 NN Validation

The results of NN training along with the training data size for each of the CASES 1–4, are shown in the Table 3 below. The columns "Target" and "Validation" present the mean value of each parameter. In Table 3, the daily-averaged coarse mode peak is measured by the volume concentration in "Radial bin 15" ($\approx 2.241\,\mu$m), the entry $\langle$AVSD$\rangle$ is the mean value of all correlations between the NN-derived AVSD and the AERONET target AVSD, and the AAOD(440 V 500) represents the regression of the satellite (from OMI) AAOD at 500 nm against the AERONET AAOD at 440 nm.

3.3.1 Microphysical outputs

For AVSD outputs related to the coarse mode, all AERONET input CASES 1–3 were able to retrieve the daily-averaged coarse volume concentration $V(c)$ and its modal peak "Radial bin 15" ($\approx 2.241\,\mu m$) to a very high level of precision: $0.967 \leq R(d) \leq 0.970$ and $0.956 \leq R(d) \leq 0.983$ respectively. The satellite input CASE 4 also retrieved the daily-averaged coarse volume concentration $V(c)$ and its modal peak but to a moderate degree $R(d) = 0.365$ and $R(d) = 0.375$ respectively. Only CASE 4 was able to retrieve the coarse mode geometric radius $r(c)$ to a moderate degree $R(d) = 0.346$. The AERONET input CASES 1–3 failed here. As described in Appendix A, this is most likely due to the fact that the AVSD of desert dust does not have a clearly defined minimum to separate the coarse and fine modes. This leads to a lot of variation in the location of the mode separation point r_s. A lack of correlation in r_s then translates into a lack of correlation in the secondary microphysical parameters like the modal geometric radii and variances that depend sensitively on it. For AVSD outputs related to the fine mode, only the satellite input CASE 4 was able to retrieve the daily-averaged fine mode volume $V(f)$: $R(d) = 0.461$. The lack of correlation with the AERONET targets for both $r(f)$ and var(f) for all NNs is due to the fact that for desert dust AVSDs, $V(f)$ is a small proportion of the total volume concentration ($\leq 9\%$). The pre-dominance of the coarse mode meant that all 4 models were able to retrieve the fine fraction (η) to a moderate degree: $0.404 \leq R(d) \leq 0.560$. The variation of $R(d)$ across the entire AVSD (not just at radial bin 15) and the daily-averaged time series of the retrieved $V(c)$ in CASE 4 are presented in Fig. 5.

Figure 5a shows moderate values of the regression coefficient ($0.340 \leq R(d) \leq 0.470$) across the whole AVSD with higher correlations ($0.438 \leq R(d) \leq 0.470$) in the fine mode: radial bins 3 ($r \approx 0.086\,\mu m$) to 7 ($r \approx 0.255\,\mu m$) and lower correlations ($0.355 \leq R(d) \leq 0.380$) in the coarse mode: radial bins 10 ($r \approx 0.576\,\mu m$) to 18 ($r \approx 5.060\,\mu m$). In Fig. 5b is shown that while there is good agreement between the mean value of the AERONET time series ($\langle V(c)\rangle = 0.342$) and the NN time series

($\langle V(c) \rangle = 0.383$) it is clear that the daily variability of $V(c)$ is not retrieved by the NN with retrieved values clamped to the narrow range: $0.2 \leq V(c) \leq 0.8 \, \mu m^3 \, \mu m^{-2}$. Finally, and importantly with respect to the AVSD, the entry "$\langle AVSD \rangle$" is the mean value of all regressions of the NN-retrieved AVSD against the target AERONET AVSD over the whole range of values of the AOD(470) – i.e. aerosol loads. In all CASES 1–4, this mean value is extremely high: $R(d) > 0.944$ – suggesting that the trained NNs were able to retrieve the AVSD despite the existence of only moderate regressions on the scale of radial bins.

Regarding the complex refractive index, CASE 1 retrieved the imaginary part CRI-I ($0.426 \leq R(d) \leq 0.473$) at all wavelengths considered, but was only able to retrieve the real part CRI-R to a lesser degree: $R(d) = 0.326$ in the near-IR (1020 nm). The addition of columnar water vapour (H_2O) in CASE 2 substantially improves the regression for CRI-R: $0.447 \leq R(d) \leq 0.565$ at all wavelengths. A marginal improvement was found in the retrieval of CRI-I: $0.437 \leq R(d) \leq 0.473$ at visible wavelengths (470–870 nm). The CASE 3 training results, despite having 4 inputs in common with CASE 2 (AOD(470), AOD(550), AOD(660) and H_2O), under-performs CASE 2 outputs with respect to retrieval of the CRI (with the exception of CRI-R(440) which showed a marginal improvement from $R(d) = 0.447$ to $R(d) = 0.476$. The NN trained with satellite inputs in CASE 4, somewhat surprisingly retrieved CRI-R to a more respectable degree: $0.521 \leq R(d) \leq 0.532$, excelling over the AERONET-input NNs. This is likely to be due to the inclusion of the modelled AAOD from OMI in the NN inputs. The satellite inputs CASE 4 NN also retrieved CRI-I at all wavelengths: $0.331 \leq R(d) \leq 0.354$, but to a lesser degree than the AERONET inputs CASES 1–2.

3.3.2 Optical outputs

In CASE 1, all optical parameters (SSA and ASYM) are retrievable with regression coefficients in the range: $0.386 \leq R(d) \leq 0.512$, with the best result being obtained for SSA(1020). The addition of columnar water vapour (H_2O) in CASE 2, while hardly impacting on the retrieval accuracy of the SSA, led to a significant improvement in

the retrieval of the asymmetry factor (ASYM) at all wavelengths: $0.630 \leq R(d) \leq 0.657$. Once again, the CASE 3 training results, despite having 4 inputs in common with CASE 2 under-performs even the CASE 1 optics outputs (with the exception of ASYM at 440 nm which is slightly better than the CASE 1 result but still worse than the CASE 2 retrieval). The addition of the 2 UV AODs in CASE 3 does not appear then to offer an improvement for dust in Northern Africa. The optical parameter retrievals of SSA and ASYM from the CASE 4 NN are, in general, moderately good: $0.322 \leq R(d) \leq 0.410$ (with the exception of SSA(440) where $R(d) = 0.262$). There appears to be a play-off between the ability of the NN to recover all microphysical parameters and simultaneously all optical parameters. The best training and validation results are associated with CASE 2 NN. In the next section we report on the performance of the CASE 1–4 trained NNs by feeding them with unseen input data, i.e. in unsupervised (testing) mode.

4 Results

The testing performance of the trained NNs was tested by feeding them with unseen CASE 1–4 input data at the coastal dust site Dakar in Northern Africa (or in the pixel containing the site in the case of satellite inputs). The test outputs are compared with the daily-averaged target AERONET microphysical AVSD (calculated at 22 equidistant logarithmic radial bins spanning the range of 0.05 μm to 15 μm), the CRI and the optical parameters SSA and ASYM at 440, 675, 870 and 1020 nm. The test results are collected in Table 4 following the same general format as the training results of Table 3. In addition to the regression coefficient for daily-averages $R(d)$, regression coefficients are also calculated for weekly-averages $R(w)$ and monthly-averages $R(m)$ so as to assess the behaviour of the NN results at other timescales.

4.1 Inputs

As for the training inputs described in Sect. 3.3, for CASES 1–2 the number of AERONET Level 2.0 Version 2 Inversion Products daily-averages at Dakar is substantially larger (862–942 records) than the 149 records available in CASE 3, and the 167 records obtained in CASE 4 due to the co-location and synchronization (the same day) of AERONET data with the satellite data. The fewer records for CASE 3 is due to the fact that relatively fewer UV measurements of AOD(380) and AOD(500) exist at Dakar. Another thing to be noted about the input data for CASES 1–4 is that outliers were deliberately not removed in the testing datasets so as to provide a more stringent test of the NN retrieval. In particular, it is important to compare the CASE 4 satellite inputs with their co-located and synchronous AERONET counterparts. This is especially important for the AAOD which is modelled from OMI, whereas from AERONET is calculated (see discussion in Sect. 3.3.2). With reference to Table 4, the regression of satellite values for AOD(470), AOD(550) and AOD(660) on their AERONET co-located and synchronous counterparts is moderate, spanning the narrow range: $0.421 \leq R(d) \leq 0.442$. A similar level of correlation is found for the AAOD(500): $R(d) = 0.450$. However a strong positive correlation is evident in the case of columnar H_2O: $R(d) = 0.834$. Figure 6 shows the daily-averaged time series of AOD(660) (as a representative measure of the aerosol optical thickness), H_2O and AAOD(500) satellite inputs overlaid on the time series of co-located and synchronous AERONET counterparts (note that the AERONET AAOD used for comparison is at 440 nm).

The MODIS and OMI data appear to be systematically lower than AERONET, particularly at higher values. This is explainable by the difference in the way AERONET's ground-based and MODIS's space-based remote sensing instruments measure the AOD. AERONET's sun photometers perform almucantar scans of light radiation based around the pointing direction to the sun (zenith angle) whereas MODIS's spectro-radiometers measure the intensity of solar radiation reflected vertically by the Earth system (the planetary surface and the atmosphere). As a result, the light

Title Page

Abstract | Introduction

Conclusions | References

Tables | Figures

◄ | ►

◄ | ►

Back | Close

Full Screen / Esc

Printer-friendly Version

Interactive Discussion

paths are usually different and sample different angular variations of aerosol (this effect is likely to be minimized when the sun is overhead but tends to increase close to sunrise and sunset). For example, AOD data from 132 global AERONET stations over a two year period were regressed against MODIS-derived AOD values and revealed MODIS values to be systematically lower than AERONET values (Remer et al., 2005). Therefore, despite its small sample size in comparison with the above study, the CASE 4 co-located and synchronous dataset at Dakar is consistent with this finding and a similar under-estimation of the satellite inputs relative to AERONET is observable (with the exception of H_2O).

4.2 Microphysical outputs

For AVSD outputs related to the coarse mode, the AERONET input CASES 1–3 were able to retrieve the daily-averaged coarse volume concentration $V(c)$ at Dakar to a very high level of precision: $0.965 \leq R(d) \leq 0.969$, and also the location of the coarse mode peak ("Radial bin 15"): $0.943 \leq R(d) \leq 0.963$. This level of accuracy is also maintained at the weekly and monthly timescales. The CASE 4 NN with satellite inputs was able to retrieve the daily-averaged coarse volume concentration $V(c)$ and its modal peak with a moderate degree of correlation: $R(d) = 0.514$ and $R(d) = 0.486$ respectively. Unfortunately, none of the NNs could retrieve the daily-averaged coarse mode geometric radius $r(c)$ or its variance $var(c)$ for reasons described in Sect. 3.3.1 regarding the problematic determination of the mode separation point for dust AVSDs. The same is true for the daily-averaged fine mode volume $V(f)$. The satellite CASE 4 NN could only retrieve $V(f)$ to a low to moderate degree: $R(d) = 0.261$ (with some improvement at the monthly timescale: $R(m) = 0.388$). CASES 1–4 present unacceptable correlations for $r(f)$ and $var(f)$ which, as described in Sect. 3.3.2, is explained by the fact that for desert dust fine particles contribute only a small proportion to the total volume concentration. Future work will present results of a NN retrieval scheme for regions dominated by other aerosol types such as urban pollution or the products of biomass burning that have a more clearly defined fine mode. With respect to the fine fraction (η),

Full Screen / Esc

Printer-friendly Version

Interactive Discussion

the dominance of the coarse mode meant that CASES 1–4 were able to retrieve this daily-averaged parameter to a moderate to good accuracy: $0.400 \leq R(d) \leq 0.491$ with the satellite CASE 4 NN retrieving η with $R(d) = 0.413$. Much stronger correlations for this parameter are evident at the monthly timescale: $R(m) \geq 0.541$. It is encouraging that the satellite retrievals for $V(c)$, its peak at radial bin 15 and also for η all show moderate correlations with co-located and synchronous AERONET outputs at the daily timescale: $R(d) = 0.514$, 0.486 and 0.413 respectively.

Finally, with respect to the AVSD, in this section the effect of increasing aerosol load (using AOD(470) as a proxy), on the AVSD regression is also briefly investigated. Low values of AOD correspond to small volume concentrations and are important to inspect due to the fact that spurious retrieval effects are known to exist at low number densities (Dubovik and King, 2000). The reason for this is that AERONET's Level 2.0 Version 2 Inversion Products are obtained following certain constraints: (i) aerosol loads should be moderate (AOD > 0.4), (ii) the sky should not have strong cloud contamination, (iii) solar zenith angles should be high (> 50°) so that the air mass factor is high, and (iv) simultaneous measurements of AOD(440), AOD(675), AOD(870) and AOD(1020) should be available within ±15 min of the almucantar measurement. When these conditions are not satisfied, inversions are less reliable or absent from the AERONET data record. Assessment of the dependence of AVSD on AOD(470) is done as follows: (1) the NN-derived AVSDs were individually regressed on co-located and synchronous AERONET AVSD targets for days sorted by AOD(470), and (2) the 20 % quantiles of AOD(470) were identified and used to calculate the mean AVSD from a sample of AVSDs corresponding to days where the AOD(470) is 10 % above and below the quantile point. Figure 7 looks into this behaviour in more analytical detail.

In the left panel of Fig. 7 showing the variation of the regression coefficient (R) with AOD(470), it is clear that the variation in the value of R decreases with increasing AOD(470). There is much greater variance in the value of R when AOD(470) $\leq$ 0.4. This is expected since, as mentioned above, AERONET retrievals are not as reliable for low aerosol loads. In the right panels of Fig. 7, the mean AVSD is calculated at

20 %, 40 %, 60 % and 80 % of the min-max range (0.01 to 1.43) of AOD(470) values. The mean NN-derived and AERONET AVSD at each quantile is calculated from a 20 % sample (10 % above and below) in the AOD(470) domain. It can be seen that for the satellite NN of CASE 4, a substantial difference is observable at the 60 % quantile level where AOD(470) = 0.865 and also at the 80 % level where AOD(470) = 1.15. However, the number of AVSDs used to calculate the mean AVSD at these quantile points is small ($N = 7$ and $N = 3$ respectively) and are not likely to be statistically representative. There is a strong resemblance between the mean AVSD obtained at the more populated 20 % and 40 % AOD(470) quantiles. Furthermore, all models (CASES 1–4) were able to retrieve very accurately the AVSD across the entire range of AOD(470) values as measured by the value ⟨AVSD⟩ (see Table 3) with mean regressions falling in the range: $0.906 \leq R(d) \leq 0.918$. It is encouraging that here, the best correlation was obtained with the satellite inputs CASE 4 NN. This brief analysis suggests that the majority of daily-averaged AVSDs retrieved with the satellite input CASE 4 NN at aerosol loads AOD(470) ≥ 0.4 appear to be reliable.

With regard to the complex refractive index, Table 4 shows that the CASE 1 NN failed to retrieve the CRI-R. It did however retrieve the CRI-I to a moderate degree: $0.406 \leq R(m) \leq 0.453$ with retrieval improving with increasing wavelength. The results for CRI-I also improve substantially at the monthly timescale: $0.651 \leq R(m) \leq 0.675$ where even CRI-R(440) also becomes acceptable with a value $R(m) = 0.375$. As described in Sect. 3.3, the addition of H_2O (i.e. the CASE 2 simulation) substantially improves the regression for CRI-R: $0.335 \leq R(d) \leq 0.410$ (with even more pronounced positive correlations at the monthly timescale). The retrieval of CRI-I is relatively unaffected by the addition of H_2O to the inputs. These test results validate our claim that H_2O is indeed an important input parameter and should be added to the base set: AOD(470), AOD(550) and AOD(660) for satellite-based retrievals. In particular, H_2O is required for moderate retrieval of CRI-R. This effect is shown in Fig. 8.

The further addition UV AOD inputs in CASE 3 did not lead to an increase in the ability of the NN to retrieve the complex refractive index. To the contrary, the

correlations were systematically worse. For the satellite inputs CASE 4 NN, the retrievals of the absorption-related CRI-I are acceptable and show a moderate correlation: $0.368 \leq R(d) \leq 0.381$. The correlation strengthens substantially at the monthly timescale and especially at shorter wavelengths: $0.469 \leq R(m) \leq 0.550$. An acceptable correlation is only observed for CRI-R(440) at the daily timescale: $R(d) = 0.344$.

4.3 Optical outputs

Referring to Table 4, the CASE 1 NN retrieves the optical SSA and ASYM parameters to a moderate degree: $0.336 \leq R(d) \leq 0.481$, with the best result being obtained for SSA(1020). In fact, for the absorption-related parameter SSA (as noted above for the CRI-I), the retrieval improves with increasing wavelength and also substantially at the monthly timescale: $0.559 \leq R(m) \leq 0.734$. The addition of H_2O (i.e. the CASE 2 simulation) leads to a minor improvement in the retrieval of the asymmetry factor (ASYM): $0.504 \leq R(d) \leq 0.516$. The correlations for SSA are relatively unaffected by the addition of H_2O. Once again, the further addition of UV AOD inputs in CASE 3 muddied the waters and failed to improve the retrieval of the optical parameters (with the exception of ASYM(440) which showed a slight improvement over the CASE 1–2 NNs at the daily timescale. For the CASE 4 NN (satellite inputs), the retrievals of the absorption-related SSA are acceptable and show a moderate correlation: $0.373 \leq R(d) \leq 0.440$. The correlation strengthens substantially at the monthly timescale and especially at shorter wavelengths: $0.521 \leq R(m) \leq 0.710$. An acceptable correlation is also observed for ASYM (440–870) at the monthly timescale: $0.304 \leq R(m) \leq 0.348$.

A visual overview of the retrieval performance of the spectrally-dependent microphysical (CRI) and optical parameters (SSA and ASYM) at the daily, weekly and monthly timescale for the satellite CASE 4 is shown in Fig. 9.

When tabulated in this "micro-array" format, one can see at a glance that the satellite input trained NN of CASE 4 retrieves the spectral behaviour of the absorption-related SSA and CRI-I parameters better than the shape-related CRI-R and ASYM parameters at all timescales. As mentioned with regard to macro-statistics, more detail is revealed

by looking at the time series of the daily-average retrievals. For example, in Fig. 10 below, daily-average retrievals of SSA(440) at Dakar are shown for the CASE 4 NN.

Figure 10 shows that the satellite retrieval at Dakar, while insufficiently fitting the magnitude of peaks and troughs in the SSA(440) time series, does echo them to some degree. Furthermore, out of the 169 co-located and synchronous daily-averages, 73.653 % (i.e. 124 of them) are within ±0.03 of the corresponding AERONET data (the target level of uncertainty suggested by Mischchenko et al., 2007). In the next section, we briefly look at the performance (in terms of the target levels of uncertainty) of the satellite input CASE 4 NN for the other retrieved parameters.

4.4 Uncertainty analysis

As mentioned in the introduction, Mischchenko et al. (2007) presented the following target levels of uncertainty for the output parameters: $r(f)$ and $r(c)$: ±10 %, var(f) and var(c): ±40 %, SSA(±0.03) and CRI-R (±0.02). In Table 5, the number of retrieved daily-averages that fall within the target band, are presented for the results of the CASE 4 test at Dakar.

In the context of the target levels of uncertainty provided, the satellite input NN of CASE 4 is performing quite well as shown by the percentage of certain simulations ("Certainty"). The retrieval of $r(c)$ is problematic (34.32 % certainty) for the reasons described in Sect. 4.2, and the retrieval of CRI-R at all wavelengths (certainties are in the low range 39.05 % to 44.97 %) is also problematic for the reasons reported above in Sect. 4.3. For all of the other parameters at least 60 % of the retrieved daily-averages are within the accepted level of difference which is a satisfactory result given the small size of the co-located and synchronous data sample at Dakar.

4.5 Timescale analysis

Here we briefly show the results of quantifying the differences between the NN outputs and the AERONET values at different timescales in order to measure the ability of the

Title Page

Abstract | Introduction

Conclusions | References

Tables | Figures

|◄ | ►|

◄ | ►

Back | Close

Full Screen / Esc

Printer-friendly Version

Interactive Discussion

trained NNs to capture temporal patterns in the data. As a measure of the typical absolute difference for each output, we calculated the median absolute error (MAE) and also the median absolute relative error (MARE). For MAE, the absolute differences between the NN outputs and the AERONET values at different timescales were calculated and the median value was then reported. For the MARE, the absolute relative error: $1-p(\text{NN})/p(\text{AERONET})$ for each parameter p at different timescales were calculated and the median value was then reported as a percentage. In the case of the AVSD, the coarse mode volume concentration $V(c)$ was used as a proxy single parameter. The MARE in particular, is a good summary measure of the typical difference between the NN model and the expected results. The results of this analysis are shown in Table 6.

With regard to the microphysics, for CASE 1–3 test results of $V(c)$ at Dakar, the use of ground-based AERONET inputs produces results that differ typically by 15.6–23.8 % from expected values (as measured by MARE). This error is comparable to reported errors for the AVSD retrieved by the AERONET inversion (Dubovik and King, 2000). The important (for this study) satellite input CASE 4 test at Dakar presents a larger error (MARE = 32.5 %). At the daily, weekly and monthly timescales, the MARE for CASE 4: are 27.6 %, 32.5 % and 24.8 % respectively. The MARE for CRI-R for all CASES 1–4 is very small and spans the range: 0.9 % to 2.2 % – indicating that the optimal NNs are simulating these parameters well (in the context of an acceptable Mishchenko uncertainty of ±0.02). Hardly any variation in the errors with timescale is observed here. However, MARE values for CRI-I reveal a very different trend. First of all, they are large compared with the MARE for the other parameters spanning the range: 34.4 % to 67.7 % for all CASES 1–4. The reason for the appearance of such significantly larger MARE values for CRI-I is that it has a very small absolute value compared to the other parameters: ⟨CRI-I⟩ ≤ 0.006. For days when the value of this parameter is particularly small (close to zero), the relative error tends towards a 0/0 type infinity error ("0/0 inflation"). Furthermore, while the impact of such outlier cases was avoided by using the median rather than the mean as a measure of the average,

clearly the results suggest that there are many "average" co-located and synchronous outputs where this effect starts to play a role around the median.

In the context of the optical parameters, the MARE for SSA, and ASYM for all CASES 1–4 is very small and spans the range: 1.0 % to 3.4 % – indicating once again that the optimal trained NNs are simulating these parameters well (in the context of an Mishchenko uncertainty of ±0.03 for SSA). Hardly any variation in the errors with timescale is observable here. Overall, the results of Table 6 suggest that it is not clear that the timescale plays an important role on the size of the typical error (apart from CRI-I where temporal averaging helps smooth out the effect of 0/0 inflation – leading to lower MARE values).

5   Discussion

A new methodology has been developed, based on a NN model, with the aim of retrieving aerosol microphysical and optics parameters from satellite remote sensing data at the daily timescale and to an acceptable degree of accuracy. The NNs were regularised and trained with AERONET Level 2.0 Version 2 Inversion Products at sites centred on the peak of dust extinction (according to the GOCART model averaged over a 10 yr period) in Northern Africa, and have been shown to be capable of learning the relationship between satellite inputs and the desired output parameters. The trained NNs have the added benefit that they retrieve the entire time series of all output parameters simultaneously. We were also able to demonstrate a new technique for objectively deducing optimal NN architectures by minimizing the back-propagation cost function over a grid of runs. Since in regression schemes like NN models, possible redundancies in both the data and the NN model space can lead to ill-posed problems, we have tried to eliminate these problems by carefully selecting data of the same aerosol type (predominantly dust as flagged up by the GOCART model global average), by constructing representative test scenarios, and by removing missing values and outliers. Furthermore, PCA was used to extract "meaningful" components from the variables in the NN

model space, to eliminate remove redundancies and to increase the performance of the NN-based retrievals.

With regard to testing the ability of the NNs to extrapolate to unseen data at Dakar, it is important to bear in mind that while an estimate of output uncertainties is provided with reference to known a priori target values, the test results presented in Sect. 4 incorporate also a network-induced error and are therefore only approximate. Having said this, the histogram of the differences between NN outputs and training targets was found to present a sharply-peaked Gaussian having a near-zero mean error. In assessing the performance of the NN model, the uncertainty accuracy requirements provided by Mishchenko et al. (2007) were shown to provide a practical guide in that they provide both limits of validity and also a context for the comparison of test retreivals with known a priori AERONET data as was seen in Table 5. In order to help summarize our findings, an overall assessment of the performance of the trained NNs at the daily timescale is shown in Table 7 below:

Assessing the performance of NNs trained on different combinations of inputs in the context of Northern African desert dust data reveals that:

1. AERONET-measured AOD inputs (470, 550 and 600 nm) alone (CASE 1) are insufficient to retrieve the daily spectral behaviour of the CRI-R simultaneously with the AVSD, CRI-I and secondary microphysical parameters, together with the optical parameters SSA and ASYM,

2. the inclusion of AERONET H_2O in the inputs substantially improves the retrieval potential of the NN, especially with respect to the daily spectral behaviour of CRI-R and ASYM,

3. the further inclusion of AERONET UV AOD (380 and 500 nm) in the inputs led to a deterioration in the performance particularly with respect to the absorption-related parameters SSA and CRI-I at the daily timescale,

4. the NN trained with MODIS AOD (470, 550 and 660 nm) and H_2O, and OMI AAOD (500 nm) was able to retrieve with a good to very good degree of accuracy the

daily-averaged AVSD as well as secondary microphysical parameters related to the coarse mode. The NN was also able to simultaneously retrieve the CRI-R (440) and the CRI-I (all wavelengths) to a moderate degree and managed to retrieve the spectral behaviour of the SSA to a moderate to good degree – but at the expense of the daily-averaged ASYM whose retrieval was poor.

6 Conclusions

The results show that it is possible to deduce an optimal NN architecture and to train it to retrieve daily-averaged aerosol microphysical and optical parameter values from satellite inputs. The acceptable performance of the NN retrieval with regard to AVSD over nearly the whole range of observed aerosol loads, means also that important secondary microphysical parameters such as the fine fraction, and the modal volume concentrations obtained are also likely to be robust and reliable (despite observed problems related to the way AERONET deduces the location of the mode separation point). The potential of the NN for retrieving size distribution information is interesting as this may open up the possibly of adding size distribution data to the arsenal of satellite products currently available.

The potential for retrieving the complex refractive index and the optical parameters, although less accurate, nevertheless can provide important information on these key parameters over regions where no ground-truth data exists. In essence, the NN model applied to satellite inputs, may allow for the creation of a virtual space-based AERONET centred at $1° \times 1°$ resolution longitude-latitude grid points over the Earth's surface.

The results presented here are appropriate to dust-dominated data over Northern Africa and further studies will assess whether or not the same methodology can be applied to other dust regions, as well as to regions dominated by other key aerosol types such as marine aerosol and the products of biomass burning and urban pollution. The NN model developed appears to offer some potential for obtaining daily retrievals

from satellite data, and it is hoped, will contribute to efforts currently underway for globally monitoring aerosols from space and hence improving assessments of global climate forcing.

Appendix A

As mentioned in Sect. 2.1.2, the secondary microphysical parameters: $r(f)$, $r(c)$, var(f), var(c), $V(f)$ and $V(c)$ need to be calculated so as to compare NN outputs with AERONET outputs. In AERONET's retrieval algorithm, all of these parameters are calculated from the AVSD by specifying a mode separation point r_s that divides the distribution into 2 volume concentrations $V(f)$ and $V(c)$. From the retrieved AVSD: $dV(r)/d\ln r$, the volume concentration V occupied by particles spanning the range of radial sizes $[r_1, r_2]$ is then calculated by integrating over the distribution,

$$V = \int_{r_1}^{r_2} \frac{dV(r)}{d\ln r} d\ln r. \tag{A1}$$

In principle, the aerosol number size distribution (ANSD): $dN(r)/d\ln r$ or $dN(r)/dr$, could equally well be used instead of the AVSD (King et al., 1978), since the conversion between the AVSD and ANSD parameters is straight-forward (see for example Appendix A of Sayer et al., 2012). Note that the AVSD is preferable to the ANSD as it is more accurate when inverting scattering properties that are more sensitive to aerosol particle volume, than number (Dubovik et al., 2011). The AERONET inversion algorithm estimates V by using Trapezium Rule integration (Dubovik and King, 2000) and the same approach was adopted in this work. The volume concentration of the fine mode $V(f)$ is obtained by setting $r_1 = 0.05\,\mu m$ and $r_2 = r_s$ while the volume concentration of the coarse mode $V(c)$ is obtained by setting $r_1 = r_s$ and $r_2 = 15\,\mu m$. The ratio of the area of the AVSD contributed to by the fine mode to the total area over the

Title Page

Abstract | Introduction

Conclusions | References

Tables | Figures

◄ | ►

◄ | ►

Back | Close

Full Screen / Esc

Printer-friendly Version

Interactive Discussion

CC BY

whole distribution constitutes the fine fraction η. The logarithmic volume geometric radius (mean logarithm of radius) measures of the characteristic size of "typical" aerosol particles in the atmospheric column sampled, and is given by,

$$\ln r_V = \frac{\int_{r_1}^{r_2} \ln r \frac{dV(r)}{d\ln r} d\ln r}{\int_{r_1}^{r_2} \frac{dV(r)}{d\ln r} d\ln r}. \tag{A2}$$

The geometric radius of the fine mode $r(f)$ is obtained by setting $r_1 = 0.05\,\mu m$ and $r_2 = r_s$ in this expression and then exponentiating, while the geometric radius of the coarse mode $r(c)$ is obtained by setting $r_1 = r_s$ and $r_2 = 15\,\mu m$ and then exponentiating. The geometric standard deviation which measures the spread of particle modes is given by,

$$\sigma_V = \sqrt{\frac{\int_{r_1}^{r_2} (\ln r - \ln r_V)^2 \frac{dV(r)}{d\ln r} d\ln r}{\int_{r_1}^{r_2} \frac{dV(r)}{d\ln r} d\ln r}}. \tag{A3}$$

The geometric variance of the fine mode $\mathrm{var}(f) = (\sigma_{Vf})^2$ is obtained by setting $r_1 = 0.05\,\mu m$ and $r_2 = r_s$ in this expression and then squaring, while the geometric variance of the coarse mode $\mathrm{var}(c)$ is obtained by setting $r_1 = r_s$ and $r_2 = 15\,\mu m$ and then squaring. From the above, it is clear that all secondary microphysical parameters depend on a precise determination of the fine mode/coarse mode separation point r_s. At present, AERONET estimates this by finding the minimum within the size interval $0.439 \le r \le 0.992\,\mu m$ (Dubovik et al., 2000). The same approach was used in this study although there are signs (see Sects. 3.3.2 and 4) that this is perhaps problematic for aerosol distributions like those for desert dust that do not have clearly separated fine and coarse modes.

Title Page

Abstract | Introduction

Conclusions | References

Tables | Figures

◄ | ►

◄ | ►

Back | Close

Full Screen / Esc

Printer-friendly Version

Interactive Discussion

References

AERONET: Level 2.0 Version 2 daily-averaged almucantar inversion products, available at: http://aeronet.gsfc.nasa.gov/cgi-bin/combined_data_access_inv, last access: 7 April 2012.

Chin, M., Rood, R. B., Lin, S. J., Müller, J. F., and Thompson, A. M.: Atmospheric sulfur cycle simulated in the global model GOCART: model description and global properties, J. Geophys. Res., 105, 24671–24, 2000.

Chin, M., Ginoux, P., Kinne, S., Torres, O., Holben, B. N., Duncan, B. N., and Nakajima, T.: Tropospheric aerosol optical thickness from the GOCART model and comparisons with satellite and Sun photometer measurements, J. Atmos. Sci., 59, 461–483, 2002.

Cybenko, G.: Approximation by super-positions of a sigmoidal function, Math. Control Signals, 2, 303–314, 1989.

Demuth, H. and Beale, M.: Neural Network Toolbox For Use with MATLAB, Mathworks, 2004.

Dubovik, O. and King, M. D.: A flexible inversion algorithm for retrieval of aerosol optical properties from Sun and sky radiance measurements, J. Geophys. Res., 105, 20673–20696, 2000.

Dubovik, O., Smirnov, A., Holben, B. N., King, M. D., Kaufman, Y. J., Eck, T. F., and Slutsker, I.: Accuracy assessments of aerosol optical properties retrieved from Aerosol Robotic Network (AERONET) sun and sky radiance measurements, J. Geophys. Res.-Atmos., 105, 9791–9806, 2000.

Dubovik, O., Holben, B., Eck, T. F., Smirnov, A., Kaufman, Y. J., King, M. D., Tanré, D., and Slutsker, I.: Variability of absorption and optical properties of key aerosol types observed in worldwide locations, J. Atmos. Sci. 59, 590–608, 2002.

Dubovik, O., Herman, M., Holdak, A., Lapyonok, T., Tanré, D., Deuzé, J. L., Ducos, F., Sinyuk, A., and Lopatin, A.: Statistically optimized inversion algorithm for enhanced retrieval of aerosol properties from spectral multi-angle polarimetric satellite observations, Atmos. Meas. Tech., 4, 975–1018, doi:10.5194/amt-4-975-2011, 2011.

Gobbi, G. P., Kaufman, Y. J., Koren, I., and Eck, T. F.: Classification of aerosol properties derived from AERONET direct sun data, Atmos. Chem. Phys., 7, 453–458, doi:10.5194/acp-7-453-2007, 2007.

GOCART: Version 4 model 3 hourly yearly model output, available at: http://aeronet.gsfc.nasa.gov/cgi-bin/bamgomas_interactive, last access: 7 April 2012.

Grubbs, F. E.: 1969. Procedures for detecting outlying observations in samples, Technometrics, 11, 1–21, 2007.

Hansen, J.: Earth's energy imbalance: confirmation and implications, Science, 308, 1431–5, 2005.

Hansen, J. E. and Travis, L. D.: Light scattering in planetary atmospheres, Space Sci. Rev., 16, 527–610, 1974.

Holben, B. N., Eck, T. F., Slutsker, I., Tanre, D., Buis, J. P., Setzer, A., and Smirnov, A.: Aeronet – a federated instrument network and data archive for aerosol characterization, Remote Sens. Environ., 66, 1–16, 1998.

Hornik, J., Stinchombe, M., and White, H.: Mutlilayer feedforward networks are universal approximators, Neural Networks, 2, 359–366, 1989.

Intergovernmental Panel on Climate Change (IPCC): Climate change 2007, the Physical Science Basis: Contribution of the Working Group I to the Fourth Assessment Report of the IPCC, Cambridge University Press, New York, 2007.

Jolliffe, I. T.: Principal Component Analysis, 2nd edn., Springer, New York, 2002.

King, M. D., Byrne, D. M., Herman, B. M., and Reagan, J. A.: Aerosol size distributions obtained by inversion of spectral optical depth measurements, J. Atmos. Sci., 21, 2153–2167, 1978.

Levenberg, K.: A method for the solution of certain non-linear problems in least squares, Q. Appl. Math., 2, 164–168, 1944.

Marquardt, D.: An algorithm for least-squares estimation of nonlinear parameters, Siam J. Appl. Math., 11, 431–441, 1963.

Mishchenko, M. I., Cairns, B., Kopp, G., Schueler, C. F., Fafaul, B. A., Hansen, J. E., Hooker, R. J., Itchkawich, T., Maring, H. B., and Travis, L. D.: Accurate monitoring of terrestrial aerosols and total solar irradiance: introducing the Glory mission, B. Am. Meteorol. Soc., 88, 677–691, 2007.

MODIS: Terra & Aqua Level 3 Collection 5.1 daily global 1° × 1° products, available at: http://gdata1.sci.gsfc.nasa.gov/daac-bin/G3/gui.cgi?instance_id=MODIS_DAILY_L3, last access: 7 April 2012.

Title Page

Abstract | Introduction

Conclusions | References

Tables | Figures

|◄ | ►|

◄ | ►

Back | Close

Full Screen / Esc

Printer-friendly Version

Interactive Discussion

Müller, D., Wandinger, U., and Ansmann, A.: Microphysical particle parameters from extinction and backscatter lidar data by inversion with regularization: theory, Appl. Optics, 38, 2346–2357, 1999.

OMI: Aura Level 3 Version 3 daily global 1° × 1° gridded aerosol products, available at: http://gdata1.sci.gsfc.nasa.gov/daac-bin/G3/gui.cgi?instance_id=omi, last access: 7 April 2012.

Picchiani, M., Chini, M., Corradini, S., Merucci, L., Sellitto, P., Del Frate, F., and Stramondo, S.: Volcanic ash detection and retrievals using MODIS data by means of neural networks, Atmos. Meas. Tech., 4, 2619–2631, doi:10.5194/amt-4-2619-2011, 2011.

Prospero, J. M., Ginoux, P., Torres, O., Nicholson, S. E., and Gill, T. E.: Environmental characterization of global sources of atmospheric soil dust identified with the Nimbus 7 Total Ozone Mapping Spectrometer (TOMS) absorbing aerosol product, Rev. Geophys., 40, 1–31, 2002.

Radosavljevic, V., Vucetic, S., and Obradovic, Z.: A data-mining technique for aerosol retrieval across multiple accuracy measures, IEEE Geosci. Remote S., 7, 411–415, 2010.

Remer, L. A., Kaufman, Y. J., Tanre, D., Mattoo, S., Chu, D. A., Martins, J. V., Li, R. R., Ichoku, C., Levy, R. C., Kleidman, R. G., Eck, T. F., Vermote, E., and Holben, B. N.: The MODIS aerosol algorithm, products, and validation, J. Atmos. Sci., 62, 947–973, 2005.

Samet, J. M., Dominici, M. D. F., Curriero, F. C., Coursac, I., and Zeger, S. L.: Fine particulate air pollution and mortality in 20 U.S. Cities, 1987–1994, New. Engl. J. Medicine, 343, 1742–1749, doi:10.1056/NEJM200012143432401, 2000.

Sayer, A. M., Smirnov, A., Hsu, N. C., and Holben, B. N.: A pure marine aerosol model, for use in remote sensing applications, J. Geophys. Res., 117, 1–25, 2012.

Schwartz, S. E.: Uncertainty requirements in radiative forcing of climate change, J. Air Waste Manage., 54, 1351–9, 2004.

Tanré, D., Herman, M., and Kaufman, Y. J.: Information on aerosol size distribution contained in solar reflected spectral radiances, J. Geophys. Res., 101, 19043–19060, 1996.

Torres, O., Bhartia, P. K., Herman, J. R., Syniuk, A., Ginoux, P., and Holben, B.: A long term record of aerosol optical depth from TOMS observations and comparison to AERONET measurements, J. Atmos. Sci., 59, 398–413, 2002.

Torres, O., Tanskanen, A., Veihelmann, B., Ahn, C., Braak, R., Bhartia, P. K., and Levelt, P.: Aerosols and surface UV products from Ozone Monitoring Instrument observations: an overview, J. Geophys. Res.-Atmos., 112, D24S47, 2007.

Table 1. Selection of desert-dust dominated AERONET sites for this work. N is the number of complete AERONET daily-averaged Level 2.0 Version 2 inversion records. For each site, the total mean extinction AOD and the percentage composition of the total is given for GOCART-modelled aerosol types.

AEROSOL TYPING	SITE	N (inversions 7 Apr 2012)	$\langle AOD \rangle$	GOCART Mean AOD & aerosol composition				
				% SO$_2$	% OC	% BC	% Sea Salt	% Dust
TRAINING (Dataset A)	Tamanrasset INM	407	0.793	4.54 %	1.39 %	0.63 %	0.13 %	93.44 %
	Agoufou	1028	0.973	3.70 %	2.47 %	0.82 %	0.10 %	92.91 %
	Banizoumbou	2283	0.920	4.57 %	3.48 %	1.09 %	0.11 %	90.76 %
	DMN Maine Soroa	680	0.967	5.27 %	3.52 %	1.14 %	0.10 %	90.07 %
	IER Cinzana	1469	0.823	4.86 %	4.62 %	1.22 %	0.12 %	89.19 %
	Ouagadougou	966	0.776	6.06 %	7.47 %	1.93 %	0.13 %	84.41 %
	Niamey	310	0.920	4.57 %	3.48 %	1.09 %	0.11 %	90.76 %
TRAINING (Dataset B)	IER Cinzana	1469	0.823	4.86 %	4.62 %	1.22 %	0.12 %	89.19 %
	Dahkla	299	0.629	8.43 %	1.91 %	0.79 %	0.95 %	88.08 %
	Santa Cruz Tenerife	660	0.405	15.06 %	2.96 %	1.23 %	4.20 %	76.79 %
	Izana	563	0.358	17.32 %	3.07 %	1.40 %	5.59 %	72.63 %
SIMULATION	Dakar	1583	0.705	7.38 %	5.53 %	1.42 %	0.71 %	84.82 %

Table 2. In this study 4 distinct optimal NN architectures were constructed corresponding to CASES 1–4. NNs for CASES 1–3 are trained on AERONET-only inputs and outputs. CASE 4 is trained on satellite inputs and AERONET outputs. The number of hidden neurons and their Tanh activation functions in NN layer 1 are in italic to distinguish them from NN layer 2 linear output neurons.

NN OPTIMISATION	PARAMETER	AERONET CASE 1	CASE 2	CASE 3	SATELLITE CASE 4
INPUTS	AOD (Visible)	AERONET AOD(470) AERONET AOD(550) AERONET AOD(660)	AERONET AOD(470) AERONET AOD(550) AERONET AOD(660)	AERONET AOD(470) AERONET AOD(550) AERONET AOD(660)	MODIS AOD(470) MODIS AOD(550) MODIS AOD(660)
	Columnar Water Vapour		AERONET H_2O	AERONET H_2O	MODIS H_2O
	Absorption AOD				OMI AAOD(500)
	AOD (UV)			AERONET AOD(380) AERONET AOD(500)	
OUTPUTS		AVSD(22 bins): 0.05–15 µm	AVSD(22 bins): 0.05–15 µm	AVSD(22 bins): 0.05–15 µm	AVSD(22 bins): 0.05–15 µm
	Microphysics	CRI-R(440,675,870,1020) CRI-I(440,675,870,1020)	CRI-R(440,675,870,1020) CRI-I(440,675,870,1020)	CRI-R(440,675,870,1020) CRI-I(440,675,870,1020)	CRI-R(440,675,870,1020) CRI-I(440,675,870,1020)
	Optics	SSA(440,675,870,1020) ASYM(440,675,870,1020)	SSA(440,675,870,1020) ASYM(440,675,870,1020)	SSA(440,675,870,1020) ASYM(440,675,870,1020)	SSA(440,675,870,1020) ASYM(440,675,870,1020)
	Training Dataset	A	A	B	A
	X = PCA (inputs); 98 % variance	1	2	2	3
	Y = PCA (outputs); 98 % variance	7	7	6	7
ARCHITECTURE	Number of Layers	2	2	2	2
	Backpropagation Method	LM	LM	LM	LM
	Cost Function	MSE	MSE	MSE	MSE
	Activation Functions (Layer 1/Layer 2)	Tanh/Linear	Tanh/Linear	Tanh/Linear	Tanh/Linear
	Optimal Neurons (Layer 1/Layer 2)	10/7	14/7	10/6	22/7
	Optimal Train %	90 %	85 %	85 %	90 %
	N (samples)	3808	3808	353	213
	N (training)	3427	3237	300	181
	N (validation)	381	571	53	32
	Train time [s]	539	1079	86	100
OUTCOME	Best Epoch	2	13	24	10
	Best training MSE	0.848	0.760	0.765	0.818
	Best validation MSE	0.714	0.629	0.552	0.719
	Pearson R ($Y = aX + b$)	0.998	0.998	0.998	0.992
	a	0.994	0.995	0.994	0.985
	b	0.000	0.000	0.000	0.005

Table 3. Training results obtained for the optimal NN found for each of the CASES 1–4. The mean "Target" outputs (AERONET) are presented along with the mean "Validation" outputs (NN) together with the Pearson product-moment correlation coefficient obtained at the daily timescale $R(d)$. The outputs are divided into microphysical parameters derived from the AVSD and the CRI, and the optical parameters SSA and ASYM.

TRAINING (NAF)		AERONET									SATELLITE		
		CASE 1			CASE 2			CASE 3			CASE 4		
		Target	Validation	$R(d)$	Target	Validation	$R(d)$	Target	Validation	$R(d)$	Target	Validation	$R(d)$
N (samples)			2099			1985			353			134	
AOD(470)			0.721			0.695			0.624			0.609	
AOD(550)			0.704			0.678			0.604			0.583	
AOD(660)			0.684			0.659			0.582			0.556	
H$_2$O						2.265			2.357			2.289	
AAOD(440 V 500)												0.061	
AOD(380)									0.621				
AOD(500)									0.650				
Microphysics	$V(f)$	0.022	0.022	−0.119	0.022	0.023	0.177	0.023	0.026	0.290	0.029	0.030	0.461
	$V(c)$	0.434	0.432	0.969	0.420	0.417	0.967	0.328	0.320	0.970	0.383	0.342	0.365
	η	0.058	0.058	0.473	0.059	0.061	0.520	0.079	0.087	0.387	0.090	0.085	0.404
	$r(f)$	0.109	0.109	0.031	0.109	0.110	0.209	0.118	0.120	0.288	0.111	0.112	0.243
	$r(c)$	2.051	2.028	0.007	2.055	2.046	0.114	1.855	1.871	0.255	2.018	1.994	0.385
	var(f)	1.139	1.135	−0.007	1.139	1.136	0.053	1.153	1.178	0.046	1.137	1.135	−0.194
	var(c)	1.560	1.562	0.158	1.563	1.569	0.166	1.584	1.572	0.346	1.534	1.560	0.268
	Radial Bin 15			0.982			0.983			0.956			0.375
	(AVSD)			0.958			0.961			0.964			0.944
	CRI-R(440)	1.472	1.466	0.068	1.472	1.467	0.447	1.475	1.472	0.476	1.448	1.446	0.532
	CRI-R(675)	1.487	1.482	0.204	1.488	1.484	0.512	1.492	1.490	0.480	1.472	1.472	0.528
	CRI-R(870)	1.471	1.467	0.276	1.473	1.470	0.546	1.481	1.481	0.484	1.464	1.465	0.521
	CRI-R(1020)	1.458	1.453	0.326	1.459	1.457	0.565	1.469	1.469	0.493	1.452	1.454	0.521
	CRI-I(440)	0.005	0.005	0.426	0.005	0.005	0.437	0.006	0.007	0.292	0.006	0.006	0.338
	CRI-I(675)	0.003	0.003	0.450	0.003	0.003	0.461	0.004	0.006	0.258	0.004	0.004	0.354
	CRI-I(870)	0.003	0.003	0.461	0.003	0.003	0.465	0.003	0.006	0.230	0.003	0.004	0.346
	CRI-I(1020)	0.003	0.003	0.473	0.003	0.003	0.473	0.003	0.006	0.220	0.003	0.004	0.331
Optics	SSA(440)	0.900	0.900	0.404	0.899	0.898	0.409	0.898	0.895	0.363	0.900	0.896	0.262
	SSA(675)	0.948	0.945	0.509	0.947	0.944	0.511	0.939	0.931	0.387	0.938	0.934	0.347
	SSA(870)	0.954	0.951	0.508	0.953	0.950	0.508	0.950	0.940	0.381	0.949	0.945	0.354
	SSA(1020)	0.957	0.954	0.512	0.956	0.952	0.510	0.953	0.942	0.379	0.952	0.948	0.351
	ASYM(440)	0.770	0.770	0.435	0.769	0.768	0.643	0.761	0.756	0.530	0.763	0.761	0.322
	ASYM(675)	0.742	0.742	0.456	0.741	0.740	0.657	0.735	0.726	0.422	0.736	0.733	0.335
	ASYM(870)	0.743	0.743	0.399	0.743	0.741	0.630	0.733	0.723	0.382	0.736	0.733	0.370
	ASYM(1020)	0.748	0.748	0.386	0.747	0.746	0.627	0.737	0.727	0.384	0.742	0.739	0.410

Title Page

Abstract | Introduction

Conclusions | References

Tables | Figures

◄◄ | ►►

◄ | ►

Back | Close

Full Screen / Esc

Printer-friendly Version

Interactive Discussion

Table 4. Test results obtained from the optimised trained NNs for CASES 1–4 using inputs from the Dakar AERONET site and satellite inputs from MODIS and OMI over Dakar.

SIMULATION (Dakar)		AERONET														
		CASE 1					CASE 2					CASE 3				
		Target	Simulation	$R(d)$	$R(w)$	$R(m)$	Target	Simulation	$R(d)$	$R(w)$	$R(m)$	Target	Simulation	$R(d)$	$R(w)$	$R(m)$
N (samples)			942					931					149			
AOD(470)			0.649					0.640					0.674			
AOD(550)			0.626					0.618					0.650			
AOD(660)			0.603					0.594					0.626			
H_2O			2.698					2.244					2.244			
AAOD(440 V 500)																
AOD(380)													0.710			
AOD(500)													0.669			
Microphysics	$V(f)$	0.026	0.026	0.115	0.279	0.581	0.026	0.026	0.209	0.290	0.504	0.033	0.027	−0.016	0.063	0.390
	$V(c)$	0.357	0.360	0.965	0.950	0.959	0.353	0.355	0.967	0.950	0.961	0.344	0.361	0.969	0.940	0.949
	η	0.092	0.079	0.474	0.599	0.762	0.093	0.085	0.491	0.600	0.812	0.115	0.082	0.400	0.446	0.706
	$r(f)$	0.115	0.118	0.043	0.227	0.344	0.115	0.117	0.029	0.152	−0.048	0.127	0.115	−0.060	−0.237	−0.703
	$r(c)$	1.928	1.909	−0.028	−0.257	0.000	1.929	1.923	0.009	0.103	0.098	1.934	1.888	−0.035	−0.151	0.151
	var(f)	1.529	1.514	−0.041	0.065	0.067	1.142	1.171	−0.065	0.018	−0.146	1.165	1.175	0.227	0.248	0.601
	var(c)	3.056	2.650	0.239	0.312	0.049	1.529	1.530	0.176	0.273	0.125	1.514	1.501	0.102	0.460	0.466
	Radial Bin 15		0.956					0.943					0.963			
	⟨AVSD⟩		0.912					0.913					0.906			
	CRI-R(440)	1.472	1.457	0.209	0.235	0.375	1.457	1.458	0.374	0.370	0.542	1.462	1.463	0.307	0.289	0.368
	CRI-R(675)	1.488	1.479	0.048	−0.058	−0.240	1.480	1.481	0.335	0.347	0.473	1.482	1.482	0.318	0.337	0.303
	CRI-R(870)	1.472	1.471	0.175	0.120	0.034	1.471	1.473	0.383	0.396	0.491	1.471	1.471	0.350	0.396	0.300
	CRI-R(1020)	1.459	1.460	0.244	0.220	0.176	1.460	1.461	0.410	0.432	0.529	1.457	1.457	0.379	0.390	0.264
	CRI-I(440)	0.005	0.006	0.406	0.437	0.651	0.006	0.006	0.395	0.427	0.585	0.007	0.007	0.208	0.214	−0.048
	CRI-I(675)	0.003	0.003	0.436	0.464	0.675	0.003	0.003	0.427	0.458	0.617	0.004	0.004	0.169	0.207	−0.004
	CRI-I(870)	0.003	0.003	0.445	0.466	0.665	0.003	0.003	0.433	0.461	0.613	0.004	0.003	0.154	0.199	−0.001
	CRI-I(1020)	0.003	0.003	0.453	0.473	0.661	0.003	0.003	0.439	0.465	0.608	0.004	0.003	0.147	0.195	−0.005
Optics	SSA(440)	0.901	0.897	0.336	0.360	0.559	0.896	0.895	0.314	0.291	0.462	0.883	0.885	0.203	0.233	−0.105
	SSA(675)	0.948	0.947	0.472	0.519	0.708	0.947	0.946	0.463	0.506	0.665	0.938	0.941	0.263	0.282	0.035
	SSA(870)	0.954	0.957	0.477	0.509	0.698	0.956	0.956	0.464	0.499	0.655	0.948	0.951	0.275	0.280	0.024
	SSA(1020)	0.956	0.959	0.481	0.507	0.692	0.959	0.958	0.466	0.493	0.643	0.952	0.955	0.277	0.276	0.004
	ASYM(440)	0.769	0.764	0.425	0.555	0.734	0.764	0.763	0.504	0.525	0.489	0.763	0.764	0.544	0.547	0.557
	ASYM(675)	0.742	0.731	0.440	0.507	0.680	0.731	0.730	0.512	0.479	0.452	0.731	0.732	0.451	0.496	0.399
	ASYM(870)	0.744	0.731	0.405	0.471	0.648	0.731	0.730	0.504	0.454	0.425	0.732	0.733	0.395	0.453	0.305
	ASYM(1020)	0.748	0.736	0.393	0.445	0.610	0.736	0.736	0.516	0.446	0.409	0.738	0.740	0.382	0.446	0.276

Title Page

Abstract | Introduction

Conclusions | References

Tables | Figures

◀◀ | ▶▶

◀ | ▶

Back | Close

Full Screen / Esc

Printer-friendly Version

Interactive Discussion

Table 4. Continued.

SIMULATION (Dakar)		SATELLITE				
			CASE 4			
		Target	Simulation	$R(d)$	$R(w)$	$R(m)$
N (samples)		167	167			
AOD(470)		0.590	0.357	0.421		
AOD(550)		0.562	0.316	0.442		
AOD(660)		0.532	0.301	0.439		
H_2O		2.419	2.779	0.834		
AAOD(440 V 500)		0.067	0.048	0.450		
AOD(380)						
AOD(500)						
Microphysics	$V(f)$	0.030	0.030	0.261	0.214	0.388
	$V(c)$	0.305	0.315	0.514	0.438	0.487
	η	0.112	0.093	0.413	0.329	0.541
	$r(f)$	0.115	0.112	−0.117	−0.296	−0.117
	$r(c)$	1.906	1.891	0.105	−0.060	0.042
	var(f)	1.137	1.134	−0.115	−0.076	−0.096
	var(c)	1.529	1.525	0.114	0.092	0.000
	Radial Bin 15			0.486		
	(AVSD)			0.918		
	CRI-R(440)	1.449	1.450	0.344	0.228	0.294
	CRI-R(675)	1.474	1.475	0.228	0.104	0.162
	CRI-R(870)	1.469	1.470	0.153	0.057	0.179
	CRI-R(1020)	1.460	1.461	0.139	0.036	0.162
	CRI-I(440)	0.007	0.007	0.381	0.347	0.550
	CRI-I(675)	0.004	0.004	0.372	0.288	0.482
	CRI-I(870)	0.004	0.004	0.373	0.274	0.486
	CRI-I(1020)	0.004	0.004	0.368	0.249	0.469
Optics	SSA(440)	0.887	0.887	0.440	0.506	0.710
	SSA(675)	0.936	0.935	0.395	0.347	0.562
	SSA(870)	0.947	0.947	0.383	0.314	0.546
	SSA(1020)	0.951	0.950	0.373	0.283	0.521
	ASYM(440)	0.757	0.756	0.159	0.120	0.331
	ASYM(675)	0.725	0.723	0.149	0.084	0.348
	ASYM(870)	0.726	0.724	0.094	0.010	0.304
	ASYM(1020)	0.732	0.731	0.067	−0.031	0.261

Table 5. Uncertainty analysis using the target levels of Mishchenko et al. (2007). Results are shown for the CASE 4 test at Dakar at the daily timescale.

MISHCHENKO PARAMETER	Uncertainty Level	CASE 4 test at Dakar ($N = 169$)			
		⟨AERONET⟩	⟨NN⟩	N Certain	Certainty
$r(f)$	±10 %	0.115	0.118	102	60.36 %
$r(c)$	±10 %	1.928	1.909	58	34.32 %
var(f)	±40 %	1.529	1.514	169	100.00 %
var(c)	±40 %	3.056	2.650	169	100.00 %
CRI-R(440)	±0.02	1.472	1.457	66	39.05 %
CRI-R(675)	±0.02	1.488	1.479	76	44.97 %
CRI-R(870)	±0.02	1.472	1.471	76	44.97 %
CRI-R(1020)	±0.02	1.459	1.460	70	41.42 %
SSA(440)	±0.03	0.901	0.897	124	73.37 %
SSA(675)	±0.03	0.948	0.947	115	68.05 %
SSA(870)	±0.03	0.954	0.957	119	70.41 %
SSA(1020)	±0.03	0.956	0.959	121	71.60 %

Title Page

Abstract | Introduction

Conclusions | References

Tables | Figures

◄ | ►◄

◄ | ►

Back | Close

Full Screen / Esc

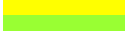Printer-friendly Version

Interactive Discussion

Table 6. Test results at Dakar obtained for CASES 1–4 for the median absolute difference (MAE) and median absolute relative error (MARE) of output parameters, at the daily, weekly and monthly timescale.

TIMESCALE ANALYSIS			AERONET									
			CASE 1						CASE 2			
	Daily (d)		Weekly (w)		Monthly (m)		Daily (d)		Weekly (w)		Monthly (m)	
	MAE	MARE %	MAE	MARE %	MAE	MARE %	MAE	MARE %	MAE	MARE %	MAE	MARE %
$V(c)$	0.081	11.6	0.093	15.6	0.072	11.5	0.079	11.6	0.090	15.2	0.062	12.0
CRI-R(440)	0.022	1.5	0.022	1.6	0.021	1.5	0.021	1.4	0.020	1.4	0.018	1.2
CRI-R(675)	0.018	1.2	0.019	1.3	0.017	1.1	0.018	1.2	0.016	1.1	0.013	0.9
CRI-R(870)	0.018	1.2	0.018	1.3	0.018	1.2	0.016	1.1	0.017	1.1	0.013	0.9
CRI-R(1020)	0.018	1.3	0.017	1.2	0.015	1.1	0.017	1.1	0.017	1.2	0.014	0.9
CRI-I(440)	0.002	34.4	0.002	35.1	0.002	36.7	0.002	42.2	0.002	42.2	0.002	40.6
CRI-I(675)	0.001	53.2	0.001	49.4	0.001	50.4	0.002	67.7	0.002	55.5	0.001	50.9
CRI-I(870)	0.001	49.1	0.001	45.5	0.001	46.9	0.001	62.9	0.001	50.2	0.001	47.7
CRI-I(1020)	0.001	47.0	0.001	44.2	0.001	39.8	0.001	59.2	0.001	49.9	0.001	44.8
SSA(440)	0.014	1.6	0.022	2.4	0.019	2.1	0.017	1.9	0.023	2.6	0.023	2.6
SSA(675)	0.014	1.5	0.017	1.8	0.017	1.8	0.017	1.8	0.020	2.0	0.019	2.0
SSA(870)	0.012	1.3	0.014	1.5	0.015	1.5	0.016	1.6	0.017	1.7	0.016	1.6
SSA(1020)	0.012	1.2	0.013	1.4	0.015	1.5	0.015	1.6	0.016	1.6	0.015	1.5
ASYM(440)	0.011	1.4	0.010	1.3	0.007	1.0	0.011	1.4	0.012	1.5	0.010	1.3
ASYM(675)	0.013	1.8	0.011	1.5	0.008	1.0	0.013	1.8	0.012	1.7	0.010	1.4
ASYM(870)	0.013	1.8	0.011	1.5	0.008	1.1	0.013	1.7	0.012	1.7	0.010	1.4
ASYM(1020)	0.012	1.6	0.011	1.5	0.007	1.0	0.011	1.5	0.011	1.5	0.010	1.3

Table 6. Continued.

TIMESCALE ANALYSIS	AERONET CASE 3						SATELLITE CASE 4					
	Daily (d)		Weekly (w)		Monthly (m)		Daily (d)		Weekly (w)		Monthly (m)	
	MAE	MARE %	MAE	MARE %	MAE	MARE %	MAE	MARE %	MAE	MARE %	MAE	MARE %
$V(c)$	0.131	13.4	0.165	23.8	0.127	11.6	0.268	27.6	0.265	32.5	0.255	24.8
CRI-R(440)	0.022	1.5	0.026	1.8	0.024	1.7	0.031	2.2	0.028	2.0	0.028	1.9
CRI-R(675)	0.017	1.2	0.024	1.6	0.018	1.2	0.022	1.5	0.022	1.5	0.023	1.5
CRI-R(870)	0.019	1.3	0.027	1.8	0.020	1.3	0.022	1.5	0.024	1.7	0.022	1.5
CRI-R(1020)	0.019	1.4	0.027	1.9	0.021	1.4	0.024	1.6	0.024	1.6	0.022	1.5
CRI-I(440)	0.002	38.7	0.002	28.0	0.003	41.9	0.002	40.8	0.002	42.1	0.002	34.6
CRI-I(675)	0.002	52.8	0.002	46.1	0.002	55.4	0.002	60.0	0.002	63.3	0.002	52.9
CRI-I(870)	0.001	42.9	0.001	44.4	0.002	52.6	0.002	60.2	0.002	63.7	0.001	59.5
CRI-I(1020)	0.001	40.8	0.001	48.8	0.002	54.5	0.002	57.0	0.002	64.1	0.001	58.2
SSA(440)	0.013	1.4	0.018	2.1	0.022	2.4	0.018	2.0	0.020	2.2	0.021	2.3
SSA(675)	0.017	1.8	0.019	1.9	0.033	3.4	0.021	2.2	0.022	2.3	0.023	2.4
SSA(870)	0.017	1.8	0.017	1.7	0.024	2.7	0.020	2.1	0.018	1.9	0.021	2.2
SSA(1020)	0.018	1.8	0.015	1.5	0.023	2.4	0.020	2.1	0.018	1.9	0.017	1.8
ASYM(440)	0.013	1.7	0.017	2.2	0.011	1.5	0.020	2.6	0.017	2.3	0.017	2.2
ASYM(675)	0.016	2.2	0.016	2.2	0.013	1.8	0.024	3.2	0.021	2.8	0.020	2.7
ASYM(870)	0.016	2.1	0.017	2.3	0.013	1.8	0.022	3.0	0.022	3.0	0.019	2.6
ASYM(1020)	0.013	1.7	0.016	2.2	0.013	1.7	0.020	2.6	0.020	2.8	0.016	2.2

Title Page

Abstract | Introduction

Conclusions | References

Tables | Figures

◀ | ▶|

◀ | ▶

Back | Close

Full Screen / Esc

Printer-friendly Version

Interactive Discussion

Table 7. Overall assessment of the simulation performance of trained NNs fed with AERONET inputs (CASES 1–3) and satellite inputs (CASE 4) at the daily timescale.

ASSESSMENT		AERONET			SATELLITE
		CASE 1	CASE 2	CASE 3	CASE 4
Microphysics	$V(f)$	Very Poor	Poor	Very Poor	Poor
	$V(c)$	Very Good	Very Good	Very Good	Very Good
	η	Good	Good	Good	Good
	Radial Bin 15	Very Good	Very Good	Very Good	Good
	CRI-R(440)	Poor	Moderate	Moderate	Moderate
	CRI-R(675)	Very Poor	Moderate	Moderate	Poor
	CRI-R(870	Very Poor	Moderate	Moderate	Poor
	CRI-R(1020)	Poor	Good	Moderate	Poor
	CRI-I(440)	Good	Moderate	Poor	Moderate
	CRI-I(675)	Good	Good	Very Poor	Moderate
	CRI-I(870	Good	Good	Very Poor	Moderate
	CRI-I(1020)	Good	Good	Very Poor	Moderate
Optics	SSA(440)	Moderate	Moderate	Poor	Good
	SSA(675)	Good	Good	Poor	Moderate
	SSA(870)	Good	Good	Poor	Moderate
	SSA(1020)	Good	Good	Poor	Moderate
	ASYM(440)	Good	Very Good	Very Good	Very Poor
	ASYM(675)	Good	Very Good	Good	Very Poor
	ASYM(870	Good	Very Good	Moderate	Very Poor
	ASYM(1020)	Moderate	Very Good	Moderate	Very Poor

Very Poor		$R(d) < 0.2$
Poor		$0.2 \leq R(d) < 0.3$
Moderate		$0.3 \leq R(d) < 0.4$
Good		$0.4 \leq R(d) < 0.5$
Very Good		$R(d) \geq 0.5$

Table 8. Acronyms.

AERONET	aerosol robotic network
AAOD	absorption aerosol optical depth
AOD	aerosol optical depth
ASYM	asymmetry factor
AVSD	aerosol volume size distribution
CRI-R	complex refractive index-real part
CRI-I	complex refractive index-imaginary part
GOCART	global ozone chemistry aerosol radiation and transport model
MAE	median absolute error
MARE	median absolute relative error
MODIS	moderate-resolution imaging spectro-radiometer
MSE	mean squared error
NN	neural network
OMI	ozone measuring instrument
PCA	principal components analysis
SSA	single scattering albedo

Title Page

Abstract | Introduction

Conclusions | References

Tables | Figures

◄◄ | ►►

◄ | ►

Back | Close

Full Screen / Esc

Printer-friendly Version

Interactive Discussion
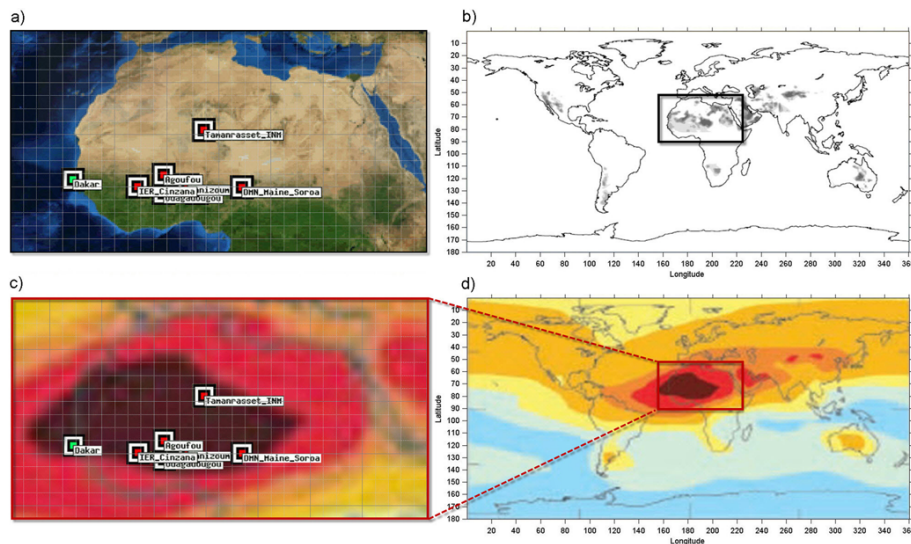
Fig. 1. Schematic showing: **(a)** the 7 Northern African (NAF) AERONET sites used for NN training (red) and the coastal AERONET site at Dakar (green) used for simulation with Dataset A, **(b)** the NAF study region in the context of the global distribution of TOMS dust sources (Prospero et al., 2002), **(c)** an overlay of the AERONET sites on the peak of dust AOD extinction for the study region extracted from the mean global GOCART model output in shown in **(d)**. (Chin et al., 2000, 2002).
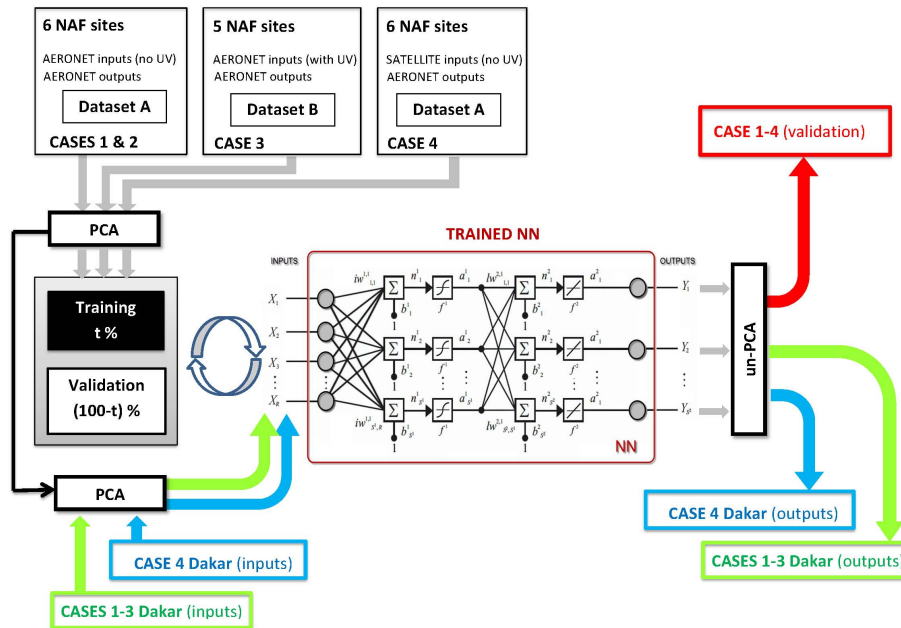
Fig. 2. Schematic of the NN model used in this work. Principal components obtained from PCA applied to CASE 1–4 data are formed and used to train the central engine NN shown in the centre. The training cycle is repeated for the grid of NNs and the optimal trained NN is found. The outputs of the trained NN are then transformed back to the full parameter space using the reverse principal components ("un-PCA"). The outputs from the trained NN are used to validate the interpolation potential of the optimal NN. Principal components obtained during the data pre-processing step of network training are used to transform new CASE 1–4 inputs at Dakar which are fed to the trained NN to simulate CASE 1–4 outputs at Dakar.
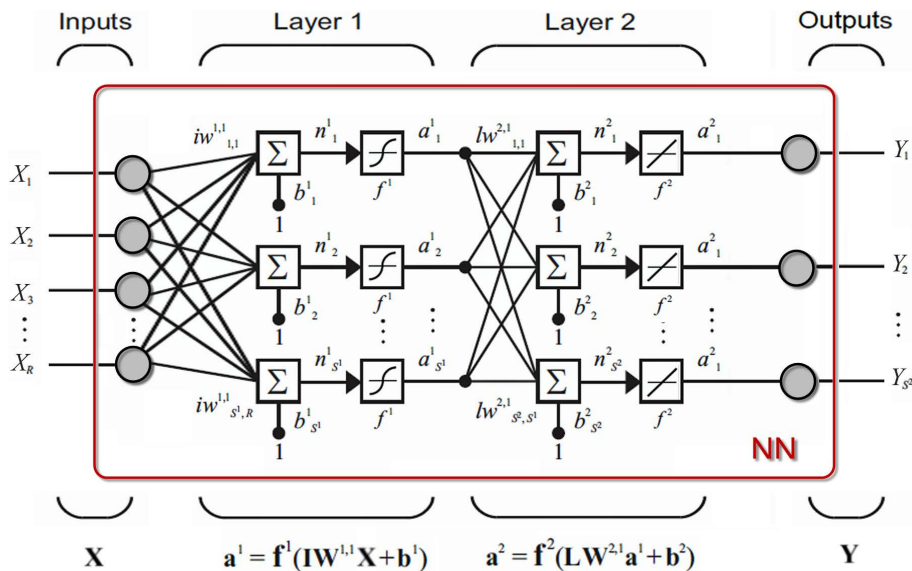
Fig. 3. Schematic showing the neural connectivity between input and output parameters.
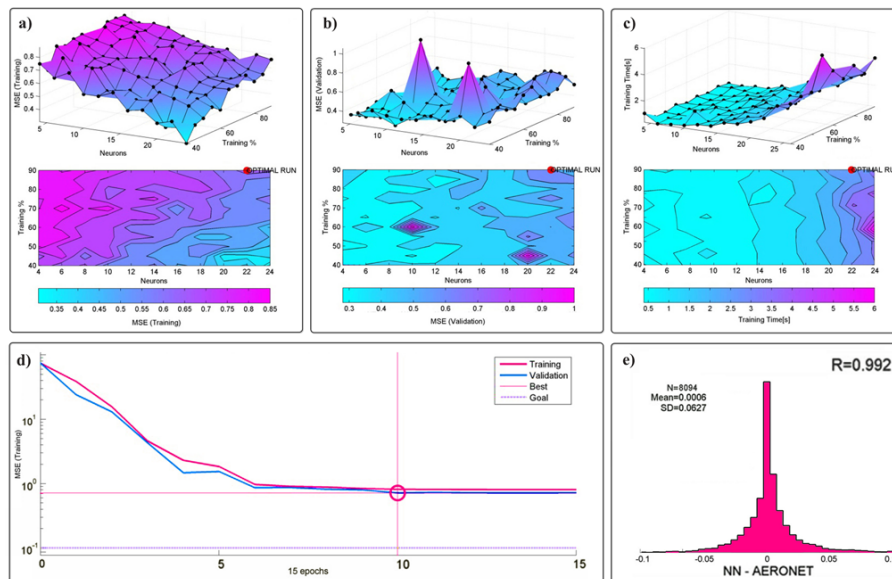
Fig. 4. Optimization of the NN for CASE 4. The upper panels show the training MSE surface (left), the validation MSE surface (middle), and the total training time surface [s] (right) for the grid of 100 NNs. The MSE of the training data and validation data (100-training %) with back-propagation iteration (epoch) is shown for the optimal NN (*22*, 90 %) in the lower left panel, while the errors calculated from the difference between the NN PC outputs and the AERONET PC outputs for the same NN together with the value of their regression coefficient *R*, is shown in the lower right panel.
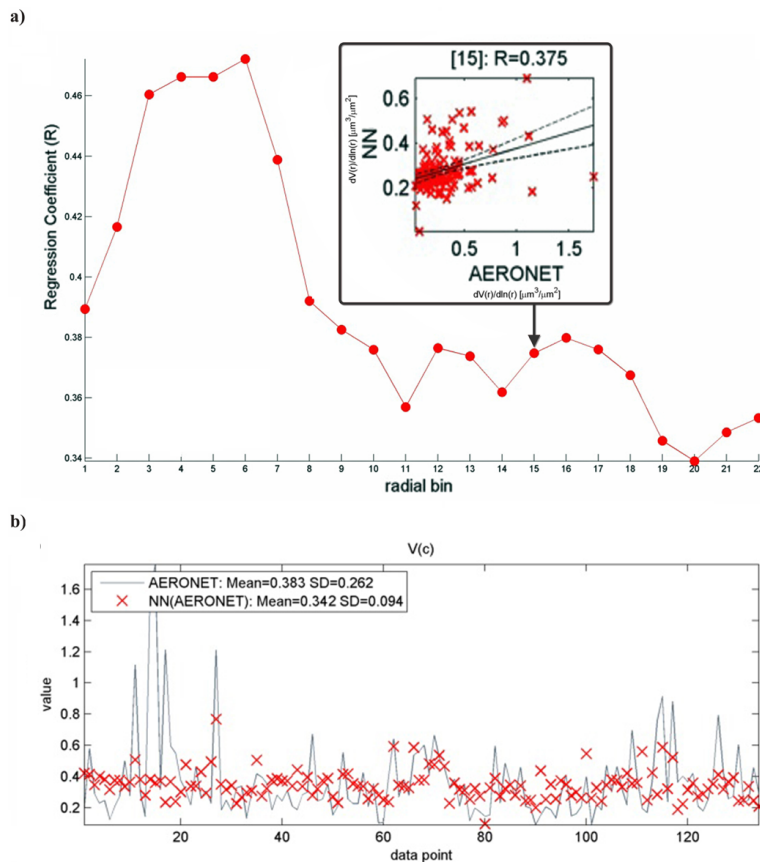
Fig. 5. Aerosol microphysical parameter training results obtained for CASE 4: **(a)** regression per radial bin of the AVSD (inset: Radial bin 15) and **(b)** daily-averaged time series for the volume concentration of the coarse mode $V(c)$.
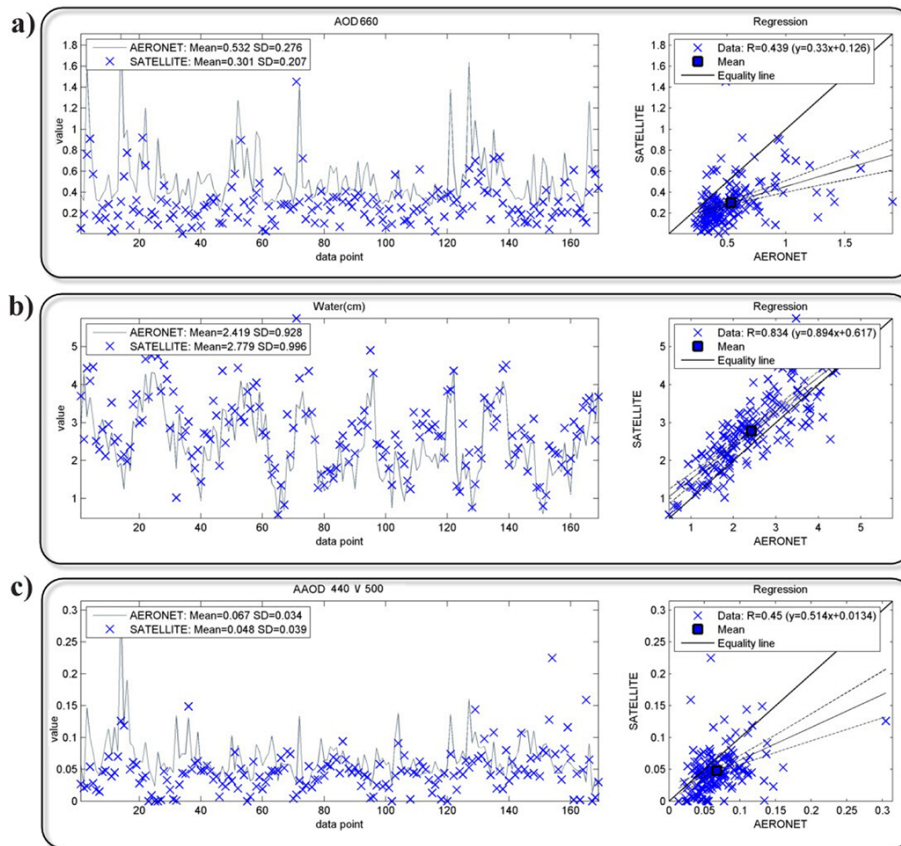
Fig. 6. Comparison of representative CASE 4 satellite inputs with co-located and synchronous AERONET values for the representative parameters: AOD(660), H_2O and AAOD(500). Mean values and standard deviations are shown for each time series together with the results of performing a linear regression.

Title Page

Abstract | Introduction

Conclusions | References

Tables | Figures

◄ | ►►

◄ | ►

Back | Close

Full Screen / Esc

Printer-friendly Version

Interactive Discussion
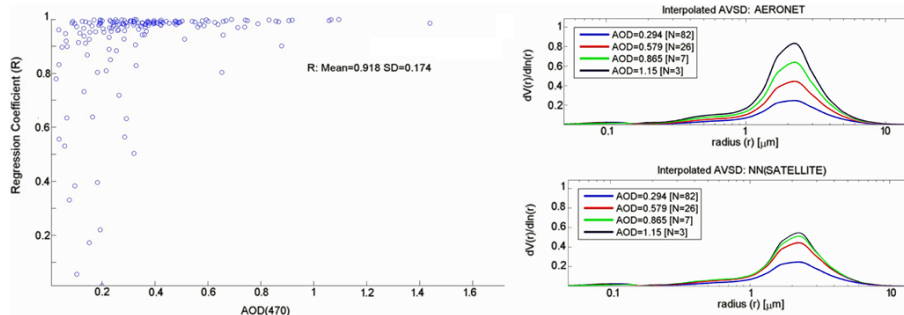
Fig. 7. Test results for the dependence of the AVSD regression on aerosol load using AOD(470) as a proxy are shown for the satellite inputs NN of CASE 4. (Left panel): each point is the regression of the 22 radial bins of the AERONET AVSD on the NN AVSD. Also shown is the AOD = 0.4 suggested limit for the validity of the results of the AERONET Level 2.0 Version 2 Inversion Products. (Right panels): the median AVSD at 20 %, 40 %, 60 % and 80 % quantile values of AOD(470).
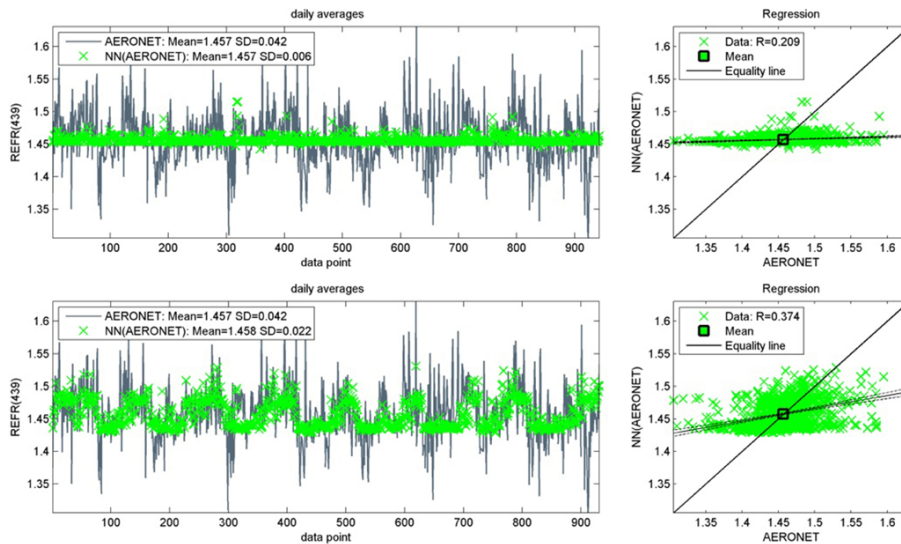
Fig. 8. Simulation results for the daily-averaged CRI-R illustrating the effect of adding columnar water vapour (H_2O [cm]) as a input (CASE 1 → CASE 2).
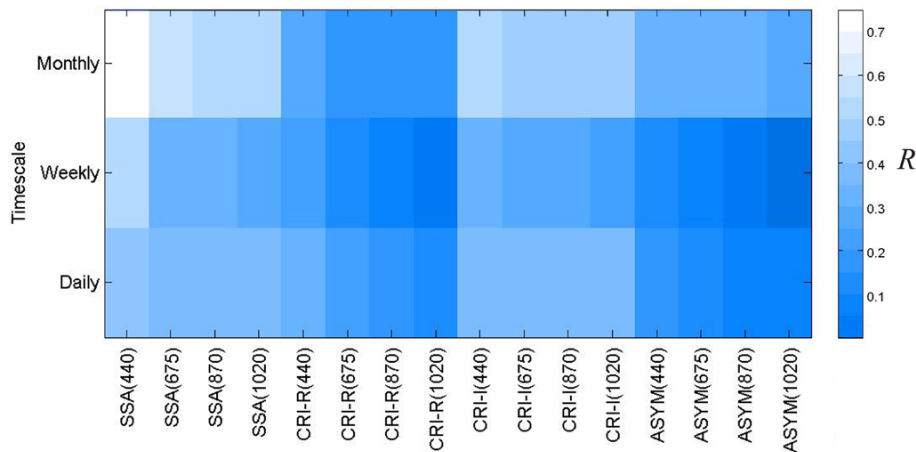
Fig. 9. Test results obtained for all spectrally-dependant microphysical and optical parameters with the satellite input CASE 4 NN at the daily, weekly and monthly timescale.
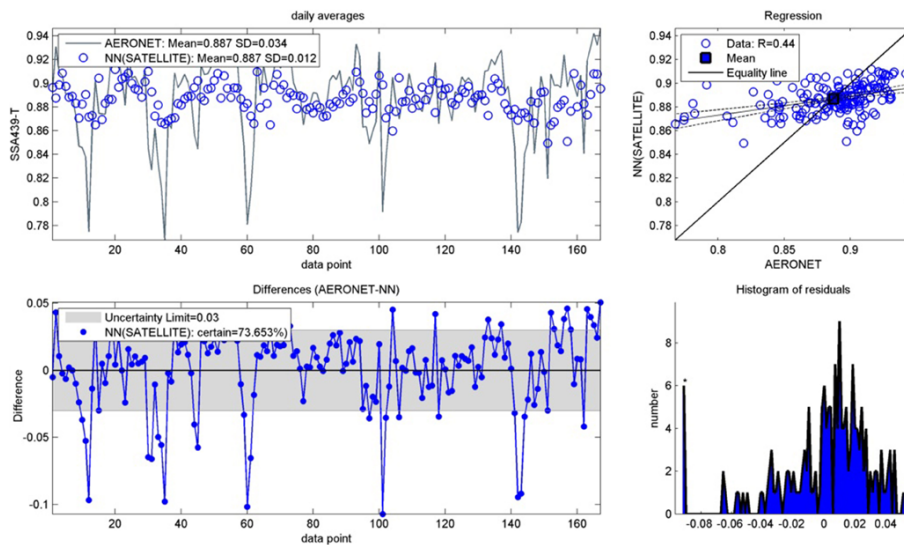
Fig. 10. Test results at Dakar for SSA(440) with the CASE 4 NN. In the lower left panel, the grey band corresponds to the desired level of uncertainty for satellite retrievals as described in Sect. 1 and discussed in Mishchenko et al. (2007). The percentage of "certain" retrievals refers to the number of retrieved daily-averages that fall within this target level.